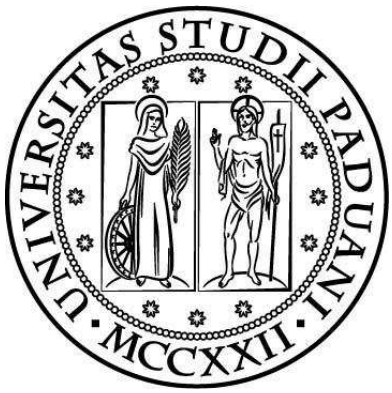

DIPARTIMENTO DI SCIENZE CHIMICHE

CORSO DI LAUREA MAGISTRALE IN CHIMICA INDUSTRIALE

TESI DI LAUREA MAGISTRALE

Synthesis, characterization and evaluation of photocatalytic activity of $BiVO_4$, TiO_2 and $BiVO_4/TiO_2$ composites.

Relatore: Dott.ssa Silvia Gross
Correlatore: Dott. Fernando Fresno Garcia
Controrelatore: Prof.ssa Marcella Bonchio

LAUREANDO: Giulia Longo

ANNO ACCADEMICO 2012/2013

Ai miei genitori

List of acronyms

AOP	–	Advanced Oxidation Process
BET	–	Brunauer-Emmett-Teller
CB	–	Conduction Band
CVD	–	Chemical Vapor Deposition
DFT	–	Density Functional Theory
DOS	–	Density Of States
DSSC	–	Dye Sensitized Solar Cells
GC-MS	–	Gas Chromatography-Mass Spectrometry
HTPA	–	Hydroxyterephthalic acid
ICSD	–	Inorganic Crystal Structure Database
PDF	–	Powder Diffraction File
PVD	–	Physical Vapor Deposition
SPD	–	Spray Pirolysis Deposition
TPA	–	Terephthalic acid
VB	–	Valence Band
VOC	–	Volatile Organic Compound
XPS	–	X-ray Photoelectron Spectroscopy
XRD	–	X-Ray Diffraction

INDEX

1. Introduction and motivations

The research of a source of energy alternative to fossil fuels, and an effective way of environmental depollution, are two of the most investigated topics of the last years. A possible solution for both these problems could be a concept born at the beginning of the XX century, which has been intensively studied during that century and became a commercialized product in the last decades: photocatalysis.

One of the first works reporting the term "photocatalysis" was published by A. Eibner in 1911, and described the bleaching of the dye Prussian blue by ZnO under illumination.[1, 2] Further works were published in the following years, reporting on the photocatalysis concept, like artificial photosynthesis of hydrocarbons (1921),[1, 3] or like the one published by Doodeve, that in 1938 reported for the first time the use of TiO_2 for photobleaching of dyes.[1, 4, 5] Nevertheless, the limited application of these discoveries quenched the interest on photocatalysis up to 1960s, when some groups started to study the photooxidation of organic compounds by TiO_2 and ZnO.[1, 6, 7]

During 1970s, due to the embargo imposed by OAPEC (Organization of Arab Petroleum Exporting Countries), the price of the crude oil skyrocketed, causing the *oil crisis*; the ghost of a future lack of fuel spurred the research on photocatalysis as method to produce alternative sources of energy.

In 1972 Fujishima and Honda published a breakthrough paper in Nature in which the photolysis of water with a TiO_2 electrode (exposed under near UV light) was reported.[1, 4, 8] This paper disclosed the door for a new way of production of clean hydrogen and, additionally, presented TiO_2 as one of the best semiconductor photocatalysts because of its chemical stability. From that moment on, the number of studies on semiconductor photocatalysis increased exponentially. During the 1980s, the research shifted from hydrogen production to pollutant degradation, as witnessed by the work of Frank and Bard in 1977 on the decomposition of cyanide.[1, 4, 9] During the following years and up to now, the attention of scientists focused on extending the knowledge of the known field of photocatalysis as well as on exploring further subfields (like photo-induced hydrophilicity or antibacterial effects), and on shifting the range of adsorption of TiO_2 to the visible wavelength.[4]

Environmental depollution was one of the most investigated fields of application of photocatalysis, both because the pollution of air and water is becoming an urgent issue, that requests fast and effective solutions, and because the depollution methods used up to now were not efficient (like active carbons, whose disposal results more complicated than the benefits they take) or they consumed large amount of energy (like incineration).[10]

Nowadays people spend more then 80% of the day time in an indoor environment, where the main pollutants are nitrogen oxides (NO_x), carbon oxides (CO, CO_2) and VOCs.[11, 12] According to the World Health Organization (WHO), VOCs are defined as all the organic substances having boiling point between 50-260 °C, excluding pesticides. Measurements carried out since 1970s, show that the concentration of VOCs is greater in indoor air than outdoor air. The sources of volatile organic compounds are numerous, but the emission from building materials is the largest one.[11]

In order to improve the indoor air quality, three paths can be followed: i) source control, ii) increasing air ventilation and iii) air cleaning. The source control is very difficult to carry out, mostly impracticable in the metropolis; increase the ventilation might diffuse outdoor pollutants in the indoor environment. For this reason air cleaning results as the easiest procedure to improve air quality.[11]

In this contest, the production of a photocatalyst able to work under indoor illumination plays a fundamental role; in particular the optimal solution would be to extend the absorption of TiO_2 to the visible range, since titanium dioxide is a candidate as ideal photocatalyst for several reasons (easy synthesis, chemical stability and inertness, low toxicity…), apart for its UV absorption. Sensitization is one of the most promising way to extend the absorption of titania. There are two classes of sensitizer: organic and inorganic ones. The former (typically organic dyes) are used in the Grätzel cells, but this type of sensitization lacks in stability, since organic molecules easily undergo redox processes. Inorganic semiconductors (generally transition metal oxides) belong to the latter class of sensitizer, and they display a enhanced chemical stability, compared with the organic ones.
For this reason the aim of this work is to sensitize TiO_2 with $BiVO_4$, and to evaluate the photocatalytic activity of this composite (under indoor illumination conditions) toward the isopropanol degradation as a model pollutant.

Since the crystalline structure is fundamental for the depollution activity through photocatalysis, it is necessary to set up and optimize easy and reproducible ways of synthesis that yield the desired phase of the two substances. In this framework, wet chemistry routes are the approach of choice, since they permit to use mild synthesis conditions and to afford the control of the different reaction parameters. Coprecipitation followed by hydrothermal treatment, coprecipitation followed by thermal treatment and a citrate-precursors (used for the production of bismuth vanadate) are the synthetic protocol routes used in this work.

In order to obtain a correlation between the composition, the structure of the photocatalysts and their activity towards air pollutant degradation, different analysis techniques were used to characterize the produced compounds.
X-Ray Diffraction (XRD) was used to evaluate the crystalline phase of the compounds and the suitability of the synthesis routes for the production of the desired compounds; X-Ray Photoelectron Spectroscopy (XPS) was used to evaluate the chemical composition of the surfaces; Brunauer-Emmett-Teller (BET) technique was applied to obtain information on the specific surface area of the photocatalysts. Furthermore, the optical behavior of the compounds was evaluated through the diffuse reflectance spectra measured using an UV-Visible spectrometer. The photocatalytic activity was determined following the reduction of a model pollutant (*i.e.* isopropanol) in a gas phase reactor through gas chromatography coupled with mass spectrometer (GC-MS). In addition, a mechanistic study was carried out by observing the formation of a fluorescent compound through a fluorimeter.

This thesis consists of six chapters. Chapter 1 is devoted to this introduction and to the motivation underpinning this work; in Chapter 2 the basic concepts of photocatalysis are explained, as well as the most important features of titanium

dioxide as photocatalyst. Chapter 3 presents a description of bismuth vanadate and titanium dioxide from a chemical, structural, electronic and optical point of view. In Chapter 4, the experimental results and their discussion are described. This fourth chapter is divided in two sections: the former describes the results obtained through the characterization techniques, while the latter one contains the photocatalytic activity evaluation of the produced materials. Chapter 5, the experimental section, provides a detailed description of the adopted ways of synthesis and of the experimental set up used during this work. In Chapter 6, a short theoretical description of the employed techniques is reported. Finally Chapter 7, presents the conclusions and the further perspectives of this work.

2. Photocatalysis

Before starting with the description of the photocatalytic process it is convenient to provide a brief description of what a semiconductor is, since in this work the photocatalytically active materials are semiconductors. When a number of atoms are combined to form a molecule, N atomic orbitals generate N molecular orbitals, half bonding and half anibonding. The difference in energy between two adjacent orbitals decreases with increasing the number of atoms. In the case of a solid with an infinite number of atoms, the ensemble of energy levels that corresponds to each atomic energy level is called energy band. Since the energy difference between the sub-levels comprising in a band is very small (≈10^{-23} eV), each band can be considered as a continuum of energy.[13]

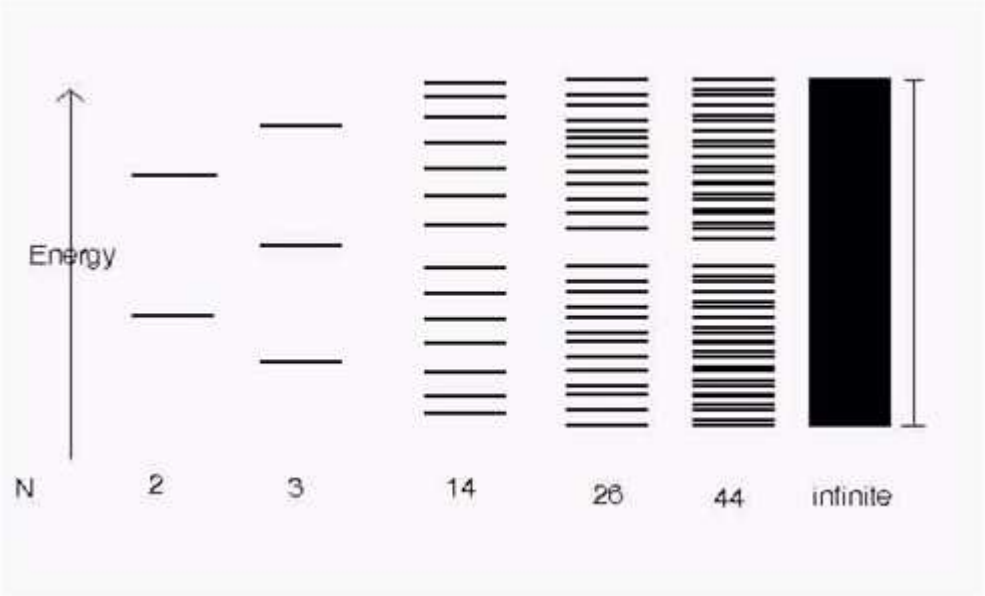

Fig. 1 Schematic representation of the band formation when an infinite number of atomic orbitals are overlapping

The band of highest energy containing electrons is defined as valence band (VB), while the lowest empty band is called conduction band (CB). The energy separation between the VB and the CB is called band gap.

There are two types of band gaps: direct or indirect. In a solid having a direct band gap, the minimum of the conduction band is directly over the maximum of the valence band; in an solid with indirect band gap the minimum of the conduction band is shifted relative to the maximum of the valence band, and the smallest interband transition must be accompanied by phonon excitation.[14] According to its band structure, a solid can behave as a conductor, an insulator or a semiconductor.

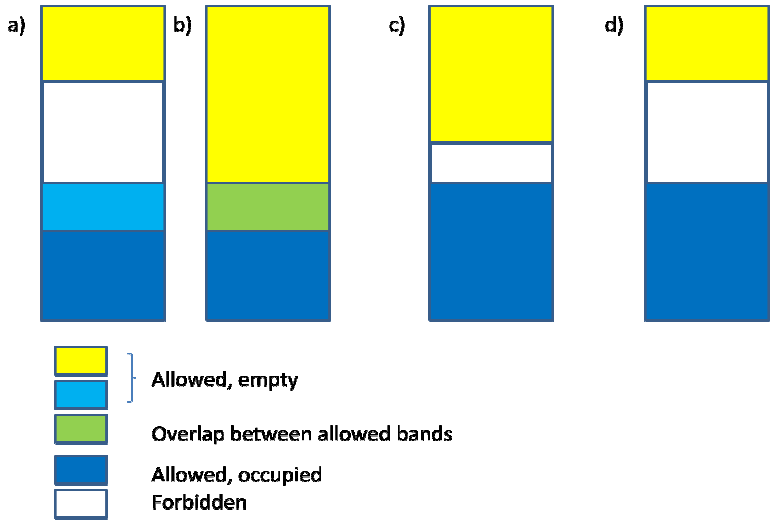

Fig. 2 Four possible band structures for a solid: a) and b) are conductors, c) a semiconductor and d) an insulator

If the valence band is only partially filled (Fig. 2a) or the allowed bands overlap (Fig. 2b), the solid is a conductor. If the allowed bands are separated by a big energy gap (generally defined as major than 4 eV, Fig. 2d) the solid is an insulator, while if the energy gap between valence and conduction band is small (usually between 1 and 4 eV, Fig. 2c) the solid is a semiconductor.[15] In a semiconductor the electrons can be promoted from the valence band to the conduction band with thermal excitation or through photoexcitation, leading (in the second case) to photoinduced phenomena.
Photoinduced phenomena is a general term to indicate all the reactions that happen thanks to a light activation of the substrate. The absorption of one photon with enough energy (it must be greater than the band gap energy of the semiconductor) permits the excitation of one electron up to the conduction band, generating a hole in the valence band.[10] If the photogenerated electrons are used in an external circuit in order to obtain work, then a photovoltaic cell is created. If the electrons and the holes are used in order to trigger a reduction or an oxidation of organic or inorganic substances, then it is a photocatalytic process. If the electrons and holes change the wettability of the semiconductor's surface, then superhydrophilicity is achieved.
The photovoltaic cells will not be treated in this work, being out of the scope of this thesis, while the photocatalytic process will be widely discussed in the next paragraphs.
Superhydrophilicity is strongly related to the photocatalytic phenomenon. Under exposure of titania to UV light, the photogenerated electrons tend to reduce Ti^{IV} to Ti^{III}, and the holes tend to oxidize the O^{2-} anions. In this process oxygen atoms are ejected and oxygen vacancies are formed. These vacancies can be occupied by water molecules, producing OH adsorbed groups which enhance the hydrophilicity. This behavior can be followed by observing the reduction of contact angle for water under UV illumination.[16]
The applications of these systems are fundamentally two: self-cleaning surfaces (houses, buildings, vehicles, paint, agriculture…), and anti-fogging properties (side-view mirrors in vehicles, houses, consumer products, optical instruments, electrical and electronic equipment…).[16, 17] Up to now these are the main fields where superhydrophilicity is applied since it is a recent discovery, but is very probable that its application will find a big spread in many further sectors.

2.1 Basic principle of photocatalysis

Photocatalysis based on semiconductors is an heterogeneous catalytic process. This implies that the process follows the five steps listed hereafter:[18, 19]

1. Transfer of the reactants in the fluid phase
2. Adsorption of the reactants on the surface of the catalyst
3. Reaction in the adsorbed phase
   - 3.1 Absorption of photons by the solid catalyst
   - 3.2 Formation of photoinduced electrons and holes
   - 3.3 Electron transfer reactions (generally formation of radicals)
4. Desorption of the final products
5. Removal of the final products in the fluid phase

The main difference between common (thermal) heterogeneous catalysis and photocatalysis is that in the latter the activation of the catalyst is not triggered by thermal activation, but rather by a photon absorption by the solid.
The process starts with the absorption of a photon with the necessary energy to promote an electron from the valence band to the conduction band. This is possible if the photon energy at least equals the band gap energy of the semiconductor, as mentioned before. The promotion of the electron leaves behind a positive hole in the valence band, which can be described as a particle.[20] Usually, the fate of these two entities (electron and hole) is to recombine, releasing the absorbed energy as emission of light or as heat. However, a small percentage of these charges does not recombine and migrates to the surface of the catalyst, promoting reactions with adsorbed molecules, starting in this way the catalytic cycle.[10, 16, 19, 21] The holes react with donors, oxidizing them, while electrons will reduce acceptor molecules (Fig. 3).

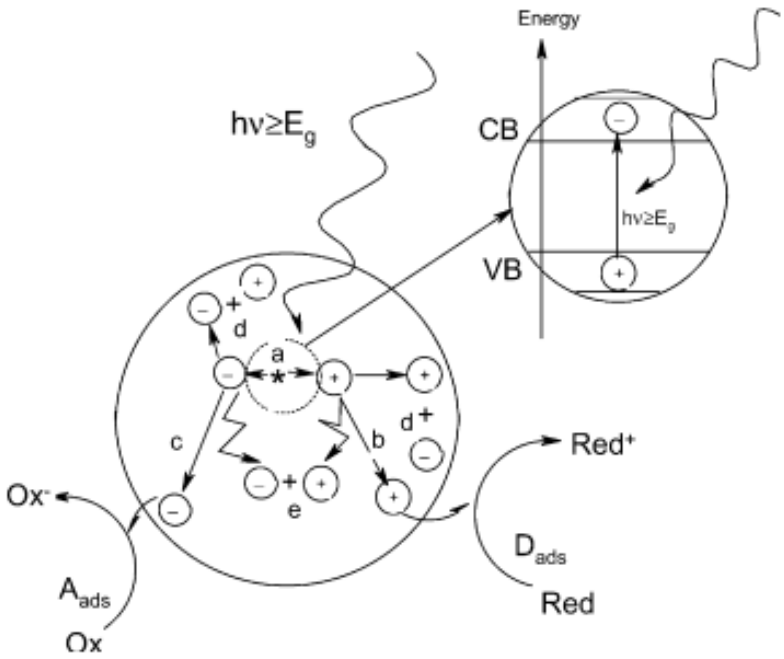

Fig. 3. Main process occurring on a semiconductor particle: (a) electron-hole generation; (b) oxidation of a donor; (c) reduction of an acceptor; (d)(e) electron-hole recombination at surface and in bulk, respectively. Figure taken from [10].

The whole process can be summarized with the following equations:

$h\nu + \mathrm{SC} \rightarrow \ \mathrm{e}^- + \mathrm{h}^+$	photogeneration of charges
$\mathrm{A(ads)} + \ \mathrm{e}^- \rightarrow \mathrm{A}^-\mathrm{(ads)}$	reduction by photogenerated electron
$\mathrm{D(ads)} + \ \mathrm{h}^+ \rightarrow \mathrm{D}^+\mathrm{(ads)}$	oxidation by photogenerated hole
$\mathrm{e}^- + \mathrm{h}^+ \rightarrow \mathrm{SC} + \mathrm{E}$	recombination

Where SC is the semiconductor catalyst, A is the acceptor (A^- the reduced form), D the donor (D^+ is its oxidized form) and E the energy released after the recombination.
The photocatalytic process can be exploited in order to obtain:

- production of H_2 to be used as fuel through water cleavage process[17]
- production of organic fuels through CO_2 reduction
- environmental depollution (both water and air) through oxidation or reduction of the pollutants
- materials with self cleaning, antifogging or anti bacterial properties

2.2 Kinetics

The photocatalytic reaction rate depends on different physical factors: i) type of catalyst, ii) mass of catalyst, iii) wavelength of irradiation, iv) initial concentration of reactant, v) specific surface area, vi) temperature, vii) radiant flux.

i) Type of catalyst.

The type of catalyst influences the rate constant for several reasons. First of all, the band gap energy between valence and conduction band is different for each type of semiconductor, and its value must allow an absorption in UV or (better) in the visible range. Nevertheless, it should be quite wide, in order to disfavor the recombination. Even if the semiconductor absorbs in the UV-Vis range, it will not be necessarily a good photocatalyst. In fact the redox potential of the photogenerated holes and electrons must be sufficiently oxidizing and reducing, respectively, in order to lead to the desired reactions.

ii) Mass of catalyst

The initial rate of the reaction is directly proportional to the mass *m* of the catalyst, as in a typical heterogeneous catalytic reaction. However, above a certain value of *m,* the rate of the reaction is independent from this parameter (Fig. 4).

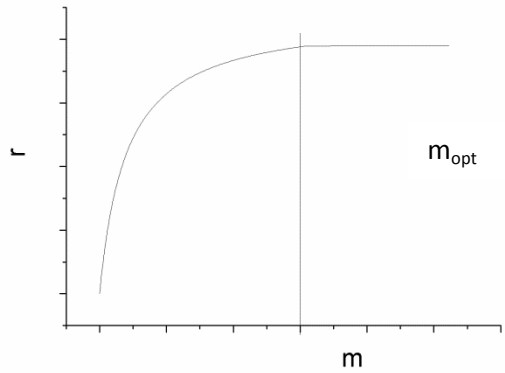

Fig. 4. Influence of the mass of catalyst *m* in the reaction rate *r*. Figure taken from [18]

The value of m_{opt} over which the rate is constant depends on the geometry and on the working conditions of the reactor, and corresponds to the highest amount of the catalyst in which all the particles (or better, all the surface exposed) are totally illuminated. Above that value, there is a screening effect, and part of the particles results masked by the more superficial ones.[18, 19]

iii) Wavelength

The rate of the reaction changes with wavelength according to the absorption spectrum of the catalyst, with the threshold related to the gap energy of the catalyst (Fig. 5).[18, 19]

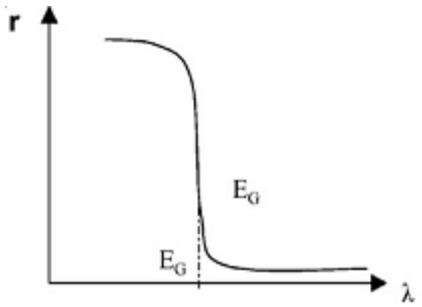

Fig. 5 Influence of the wavelength *λ* in the reaction rate *r*. Figure taken from [18].

iv) Initial concentration of reactant

Being photocatalysis an heterogeneous catalytic process, it often obeys to the Langmuir-Hinshelwood rate equation. For a generic bimolecular reaction, in heterogeneous catalysis:

$$A + B \rightarrow C + D$$

The rate constant is expressed as:

$$r = k\theta_A\theta_B$$

Where θ_i is the coverage of the generic reactant i, that varies as

$$\theta_i = \frac{K_i X_i}{1 + K_i X_i}$$

K_i is the adsorption constant of the species i, while X_i is either the concentration in the liquid phase or the partial pressure in the gas phase of the species i.
So the rate of the reaction results[18]:

$$r = \frac{kK_AK_BX_AX_B}{(1 + K_AX_A)(1 + K_BX_B)}$$

Generally one of the reactants is in excess, so that it can be considered constant, therefore θ_B=constant. The rate equation becomes:

$$r = k\theta_A\theta_B = k'\theta_A = \frac{k'K_AX_A}{1 + K_AX_A}$$

In the case that the initial concentration is much lower than the maximum value, that corresponds to the reaching of the plateau, an approximation can be made, that is: $\theta_A \approx K_AC_A$. In this way the rate form becomes an apparent first order reaction:

$$r = k'K_AC_A = k_{app}C_A$$

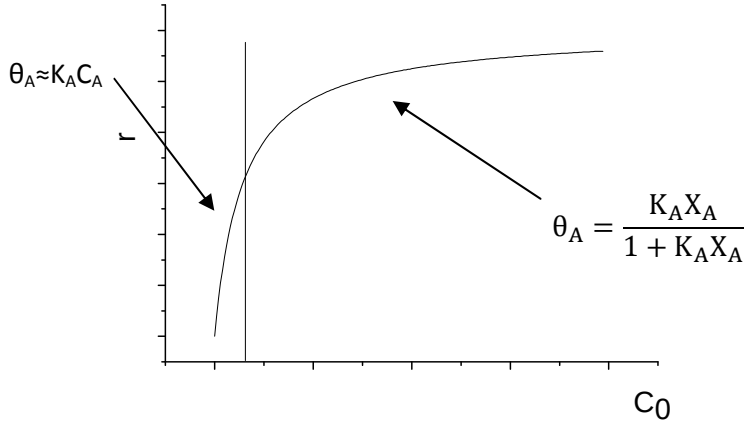

Fig. 6. Influence of initial concentration of the reactant C_0 in the reaction rate *r*.

v) Specific surface area

The specific surface area of the catalyst influences the reaction rate changing the amount of the initial reactant adsorbed on the semiconductor surface. In fact, the higher is the specific surface area, the highest is the number of molecules that can be adsorbed on the surface, and this changes the reaction rate as seen in the previous point.

vi) Temperature

In photocatalysis the true rate constant k seen in the previous paragraph is independent from the temperature and only depends on light intensity (as explained below). This is due to the fact that there is not a thermal activation of the catalyst, substituted by a photo-activation; that is, phonons have been replaced by photons.[18] However the temperature influences the adsorption constant, according to the Van't Hoff's law:

$$K_i = (K_i)_0 \exp\left(-\frac{\Delta H_i}{RT}\right)$$

So, since adsorption is a spontaneous exothermic phenomenon, low temperatures enhance adsorption, including the adsorption of the products of reaction, that work as inhibitors, while too high temperatures leads to a lower adsorption of the reactants, as shown in Fig. 7. The optimal range to work in general results between 20°C and 80°C.[19]

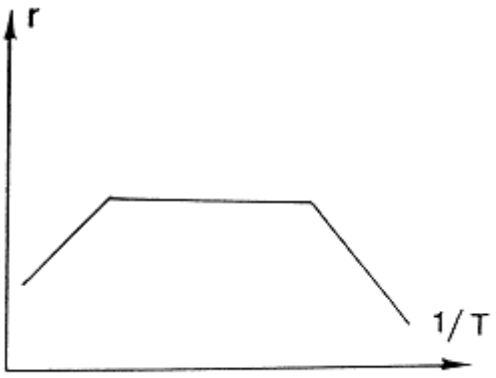

Fig. 7. Influence of the temperature *T* in the reaction rate *r*. Picture taken from [19].

vii) Radiant flux

The rate of the reaction is initially directly proportional to the radiant flux ϕ but, above a certain value, it varies with the square root of ϕ, that is r = f($\phi^{1/2}$), as shown in Fig. 8. In fact, if the radiant flux is too high, the identical quantities of holes and electrons generated are greatly increased, and this leads to a parabolically increasing of the recombination rate constant.[18, 19]

$$r_R = k_R[e^-][h^+] = k_R[e^-]^2$$

Furthermore, an increase in the radiant flux can lead to a heating of the catalyst, moving to the left side of the graph in Fig. 7, and causing a further decrease of the rate.

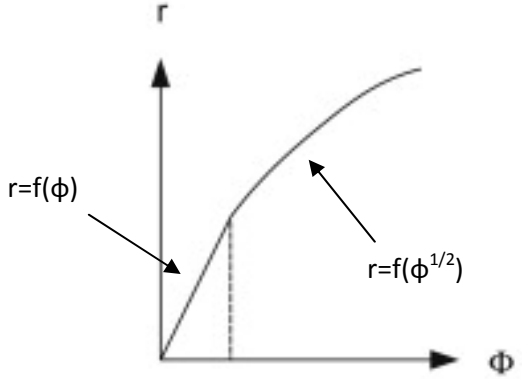

Fig. 8. Influence of the radiant flux *Φ* in the reaction rate *r*. Picture taken from [18].

2.3 Photocatalysis for air depollution

The main organic pollutants in air are volatile organic compounds (VOCs).[11, 12] There are two classic methods to remove them from air: i) non combustion processes and ii) combustion processes. With the former, the VOCs released from the waste gas are collected by adsorption, condensation, biological filtration; this techniques present several limitations in practical applications. Active carbons, for example, display a completely different adsorption efficiency with the temperature change. Furthermore, their disposal creates also some problems. With the latter method, VOCs are destroyed by thermal or catalytic incineration, but this method consumes significant amounts of auxiliary fuel and energy. For these reasons the photocatalytic activity of titanium dioxide (and other semiconductors) in gas phase reactions has caught the attention of industries and researchers.[10]
Compared with other air depollution strategies, gaseous photocatalysis has pros and cons, and the performances of the catalyst are not always the same, but they change depending on the pollutant. The pros compared with other methodologies are:

- it can work at low temperatures and pressures, but it is not limited to these values;
- a photocatalytic reactor may be integrated in a new or already existing ventilation, heating or conditioning system;
- it offers potential utilization of solar energy;

The cons of photocatalytic air depollution are:

- with some pollutant an incomplete mineralization is achieved;
- the products of degradation of some molecules can be more toxic than the initial substrate (such as phosgene from trichloroethylene, for instance).[10]

In this work the target air pollutant is isopropanol. The path of degradation can be schematically summarized in the picture below.

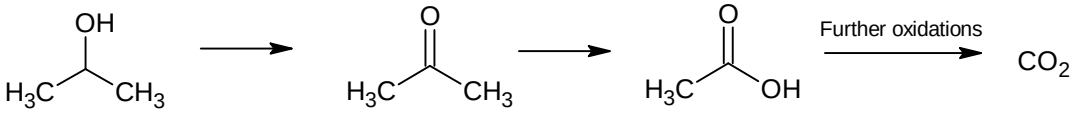

The first product of the degradation of isopropanol is acetone; anyway acetone is just an intermediate, and its concentration reaches a maximum with time and then starts to decrease.[22, 23]

2.4 TiO_2 as a photocatalyst

Among the different semiconductors with photocatalytic activity, titanium dioxide is surely the most studied one.[10, 16, 24] An ideal semiconductor photocatalyst should be:

1. photoactive
2. able to utilize near UV or visible light
3. biologically and chemically inert
4. photostable
5. inexpensive
6. non toxic

Titania meets all these requirements, except for the region of absorption, that is the UV region.[25] This is due to its electronic structure; the band gap of the anatase phase is 3.2 eV (*i.e.* 387 eV), and this means that it absorbs in the limit of the UV region. Since UV radiation corresponds to only approximately 4% of the whole emission spectrum of the sun, titania is not the best photocatalyst to work under solar light.

The main pathway of the photomineralization of organic compounds can be summarized with the following reaction:

$$\text{Organic compound} \xrightarrow{TiO_2} CO_2 + H_2O + \text{mineral acid}$$

If the initial compound has not heteroatoms, the products of the total mineralization are just carbon dioxide and water; if the organic compound contains some other atoms except for carbon, hydrogen and oxygen, the total mineralization will lead to CO_2, H_2O and to an acid depending on the type of heteroatoms (HCl, HBr…).

The detailed mechanism of reaction of TiO_2 is still not completely clear, and it is a source of debate. As already mentioned, the process starts with the absorption of photons, that creates a charge separation. This is followed by two possible mechanisms: the direct reaction of the charges with the organic substrate or the transfer of the charges to some mediators. The first one seems to have more importance when the coverage is very high. In any case both photocatalytic oxidative and reductive reactions occur simultaneously, in order to avoid the building up of a charge.[10] It seems that both routes are possible, but the reduction/oxidation by some species that accept the charges is believed to be the predominant way.

In this mechanism, the holes react with water adsorbed on the surface or with the titanol surface groups (-TiOH), generating hydroxyl radicals (Ti^{IV}-OH·); also electrons generally react with Ti^{IV}-OH groups, reducing them to Ti^{III}-OH. The reduced species can react with oxygen giving the superoxide O^-_2.

Theoretically, the redox potential of the photogenerated charges is able to produce H_2O_2 by water oxidation or by two-electron reduction of the adsorbed oxygen. The hydrogen peroxide can behave as a direct source of hydroxyl radicals or as an acceptor of the photogenerated electrons. Depending on the experimental conditions the holes, hydroxyl radicals, superoxide, peroxide and oxygen can have a different role in the photodegradation mechanism.[10, 16, 24, 26]

Since valence band has a redox potential much more oxidizing than the reducing power of the conduction band, the depollution occurs thanks to oxidation reactions, so this type of degradation of organic pollutants can be included in the so-called AOP, Advanced Oxidation Processes.[18]

As it has been shown, titanium dioxide is the semiconductor closer to the ideal photocatalyst, apart from the limited visible light absorption. For this reason, tremendous efforts have been made in order to extend the photocatalytic activity of titania to visible light irradiation.

The main strategies followed to achieve this are: a) non metal doping, b) metal doping, c) sensitization, shortly described below.

a. Non-metal doping

It is based on the introduction of a non metal element in the TiO_2 lattice structure, in order to shift the absorption to the visible region. The most common incorporated element is nitrogen which, thanks to the similar size with oxygen, can act like a substitutional element in the oxygen lattice sites or at interstitial lattice sites. The N-doped titania seems more active in the visible region because the anti-bonding π^* N-O orbitals between the TiO_2 valence band and conduction band are believed to facilitate the absorption, acting as a stepping stone for excited electrons between conduction and valence bands. Anyway there are contrasting opinions about this.[24 27]

It is also possible to use different non metal dopants, but with different effects. In fact another effort made by the researchers to enhance the photocatalytic activity under solar irradiation does not consist in a shift of the band gap to lower energies, but in a improvement of the photocatalytic activity under UV, in order to maximize the efficiency obtained using just the 4% of the solar spectrum. In this respect an example of other non-metal dopant is fluorine. It does not change the band gap, but it increases the superficial acidity of TiO_2, and causes the formation of reduced Ti^{3+} ions. Thus the charge separation is promoted and the efficiency of photoinduced processes under UV is improved.[24] Also physical modifications of TiO_2, in order to increase the surface area or the porosity, can help to enhance the photocatalytic activity.

b. Metal doping

It consists in a controlled doping by introducing a metal (generally a transition metal) or a transition metal ion in the structure of titania. The incorporation of transition metals (or their ions) may lead to the formation of a state between the valence band and the conduction one in titanium dioxide, inducing a shift in the light absorption; anyway it is still not sure that metal doping can improve the photocatalytic activity. In fact the metal centers can also act like a recombination sites, decreasing the lifetime and, consequently, the quantum efficiency.[10, 24]

A common example is doping with transition metal having d^5 configuration, as Fe^{3+}. It has half filled electronic configuration that makes the cation particularly stable. When the metallic center traps the electron, the cation is destabilized, and the electron is easily transferred to the absorbed mediators on the surface of the catalyst, so that the metallic ion can return to the five electrons configuration.[10]

The incorporation of a noble metal (like Ag, Au, Pt or Pd) on the catalyst surface, instead, does not create a new energy level, but improves the photocatalytic efficiency under visible light favoring the interfacial charge transfer (and therefore delaying the electron-hole recombination), since the noble metals act as an electron trap.[24, 28]

c. Sensitization

Photosensitization is the process by the which a photochemical or photophysical alteration occurs in one species (molecule or solid) as result of initial absorption of radiation by another species called photosensitizer.[29] Regarding semiconductors, photosensitization is most known with some organic molecules, typically dyes, which indeed represent the basic functional mechanism of the dye-sensitized solar cell (DSSC).[30] In photocatalysis this type of semiconductor sensitizing presents some

disadvantages, since the organic molecules can undergo oxidation/reduction reactions which may result in low stability of the system.
Alternatively, inorganic sensitization may be attained by heterostructuring, that is coupling two semiconductors in order to promote the separation of photoexcited electron-hole pairs. This implies the formation of a p-n junction, that permits the re-equilibration of the Fermi levels. This means that the electrons will migrate from the semiconductor with the highest conduction band to the semiconductor with the least energetic one, while holes will pass from the lowest valence band to the highest energetic one (Fig. 9).

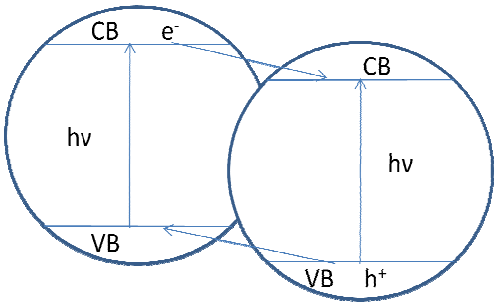

Fig. 9 Semiconductors coupling

If one of the semiconductors absorbs in the visible region it can behave like a sensitizer for the semiconductor with the UV-only absorption.[1] Let us call A the semiconductor that is excited by visible light, and the other one B.
If the conduction band of A is higher than the conduction band of B, then A will pass the excited electrons to B (Fig. 10, i).
If B has higher valence band than A, A will pass the holes to B (Fig.10, ii).

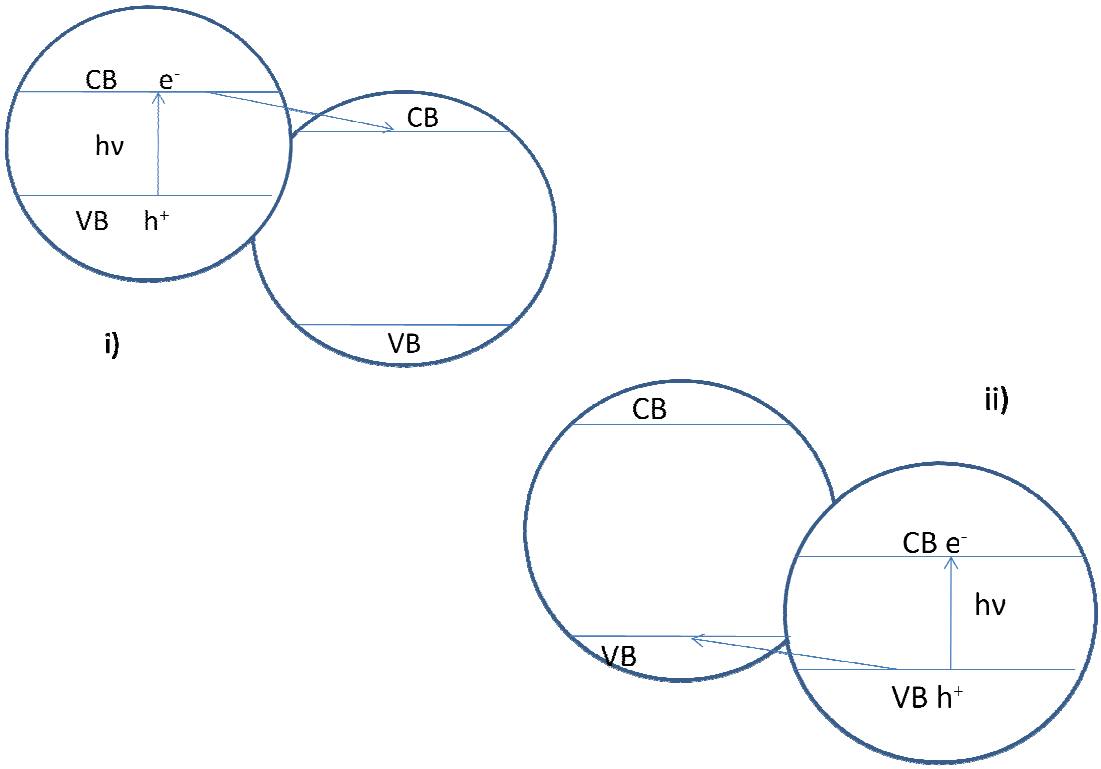

Fig. 10 Representation of heterostructuring of two semiconductors with different band gap. i) Sensitizer with higher CB than titania. ii) Sensitizer with lower VB than titania

In the case of this work, $BiVO_4$ was chosen like a sensitizer of titania, transferring electrons from the sensitizer to the substrate on the titania surface.[24] This is true if the conduction band of $BiVO_4$ is higher than the conduction band of TiO_2; if this condition is not fulfilled, then the sensitizer will pass to titania the holes formed after photoexcitation of the electrons. In literature this aspect represents an open debate: Hu et al. claim that conduction band of bismuth vanadate is higher than the conduction band of titanium dioxide, and therefore the vanadate must transfer the excited electrons to the conduction band of titania.[31] However this would mean that the conduction band of $BiVO_4$ should have a more negative reduction potential (the electrons should be more reducing) than the conduction band of TiO_2, that is -0.52 eV.[16] Consequently bismuth vanadate should be able to produce H_2 from water, but it does not, as shown by Kudo et al.[32] Within this hypothesis the holes will be transferred from the sensitizer to the titania, not the electrons as stated before.

3. Addressed systems

3.1 Bismuth vanadate ($BiVO_4$)

Crystal structure

Bismuth vanadate exists in nature as the mineral pucherite, with an orthorhombic crystal structure. There are also other two polymorph phases, that are clinobisvanite (monoclinic structure) and dryerite (tetragonal structure).[1] The $BiVO_4$ synthesized in laboratory occurs in a scheelite or a zircon type structure. The former one can have a tetragonal crystal structure or a monoclinic one, while the latter one has a tetragonal crystal structure.[1, 33] In the scheelite structure, the basic structural unit is formed by VO_4 tetrahedra and BiO_8 dodecahedra. Each vanadium atom is surrounded by four atoms of oxygen, and each bismuth atom is surrounded by eight oxygen atoms, each one belonging to a different VO_4 tetrahedron.

The difference between the tetragonal and the monoclinic crystal system is that in the latter one the local environment of vanadium and bismuth atoms are distorted, removing the four-fold symmetry typical of the tetragonal system. This is confirmed also by the measurements of the bond length: the four V-O bonds have the same length (1.72 Å) in the tetragonal phase, while in the monoclinic scheelite two different V-O lengths exist, 1.77 Å and 1.69 Å[33].

In the zircon type structure vanadium is still surrounded by four oxygen atoms, and bismuth by eight oxygen atoms, but these belong to only six VO_4 tetrahedra, because two of these tetrahedra share two atoms of oxygen, instead of one as in the scheelite structure.

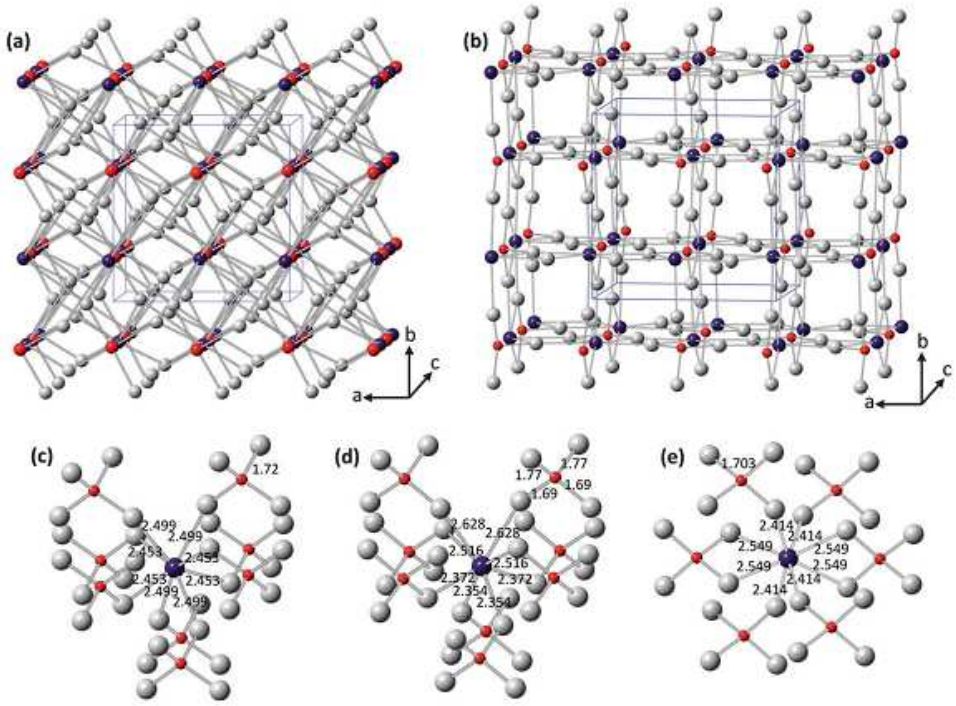

Fig. 11 Crystal structures of (a) tetragonal and (b) zircon-type $BiVO_4$ (red: V, purple: Bi, gray: O). The monoclinic scheelite structure is very similar to (a) with the exception being the subtle changes in atomic positions of Bi, V, O. Local coordination of V and Bi ions in (c) tetragonal scheelite, (d) monoclinic scheelite and (e) zircon-type $BiVO_4$ structures with bond length reported in Å. Figure taken from [33]

Among this three structures, the monoclinic scheelite is the most photoactive one.[33-43] The enhanced photoactivity in the visible region of the monoclinic scheelite type over the tetragonal zircon-type structure is due to the band gap energies, respectively 2.4 eV e 2.9 eV, that allow the monoclinic $BiVO_4$ to absorb in the visible region. The band gap energies of the two scheelite structures are very similar but, also in this case, the monoclinic system is the most photoactive. This is likely due to the distortion of the metal polyhedra that enhances the local polarization, which favorably affects the electron-hole separation, enhancing the photoactivity[41].

In particular, there is a distortion of the VO_4 tetrahedra that moves the location of the positive and negative charges from the same point to different ones, creating in this way an internal electric field, that causes the improvement of the photoactivity for the above mentioned reasons.

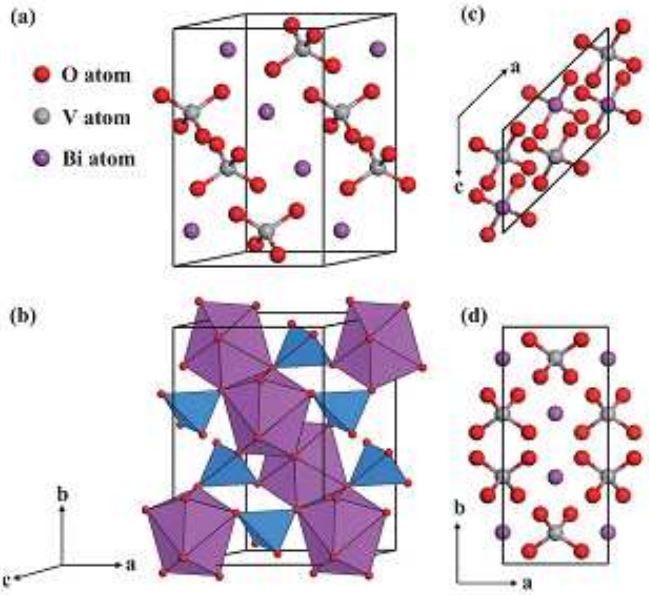

Fig. 12 (a) The crystal structure of monoclinic clinobisvanite $BiVO_4$. The corresponding polyhedron structure is represented in (b) (VO_4 tetrehedron in blue, and BiO_8 dodechaedron in purple). The top view (c) and side view (d) of the structure are also given. Figures taken from [42]

Electronic structure

Bismuth vanadate is a semiconductor. Its band gap energy allows it to be active in the visible region, with values of 2.4 eV for the scheelite structure and 2.9 eV for the zircon type structure, as mentioned above. The electronic structure of this compound is still not well defined, and in the literature different descriptions of it can be retrieved. The density functional theory (DFT) calculations performed by Walsh et al.[43] show that the smaller band gap of monoclinic bismuth vanadate, compared with the zircon type, is due to an hybridization between the Bi 6s state and the O 2p states at the top of valence band; this interaction has an antibonding nature. The conduction band is formed principally by V 3d states, with the contribution of O 2p and Bi 6p.[1] These calculations show also that $BiVO_4$ has a direct band gap. A more recent DFT study made by Zhao et al.[42] reports some differences in the electronic description of $BiVO_4$. The top of the valence band is predominantly formed by the non bonding O 2pπ states, with the contribution of Bi $6s^2$, while the conduction band is formed mostly by V 3d states, with the contribution of O 2p and Bi 3p.

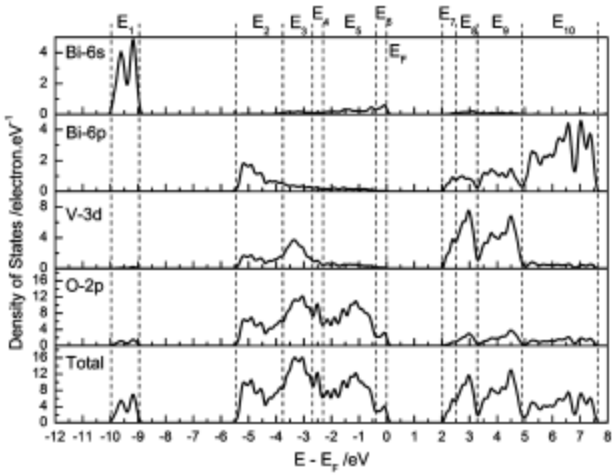

Fig. 13 total and local partial density of states of monoclinic clinobisvanite $BiVO_4$. The DOS is decomposed into the main electron states of each component. The vertical dashed lines are used to distinguish different energy ranges. Figure taken from [42]

Another difference is that they found out that the minimum gap is an indirect band gap, but with the presence of also direct band gaps that are only slightly bigger than the indirect band gap. Since there is this uncertainty in the type of band gap, in the next treatment of the data both direct and indirect band gaps of bismuth vanadate will be calculated from UV-Vis spectra.

Optical properties

Bismuth vanadate is commonly used in the industrial dyes branch since it has an intense yellow color. It has a strong optical anisotropy; in fact the optical properties calculated for the polarization direction $\vec{E}//\vec{a}$ and $\vec{E}//\vec{c}$ are mostly the same, while the properties calculated from $\vec{E}//\vec{b}$ directions are completely different. This anisotropy derives from its crystal structure: there are two different lengths of V-O bonds and four different lengths of Bi-O bonds. In addition, along the three axes, the arrangement of bismuth and vanadium atoms is different. Along the *a*-axis and the *c*-axis, there is alternation of the two kinds of atoms, that is -Bi-V- repetition, while along the *b*-axis the configuration is –Bi-V-V-Bi-. This leads to different dipoles along the *b*-axis, thus electron transitions are forbidden along the polarization direction $\vec{E}//\vec{b}$, while they are allowed along $\vec{E}//\vec{a}$ and $\vec{E}//\vec{c}$ directions.

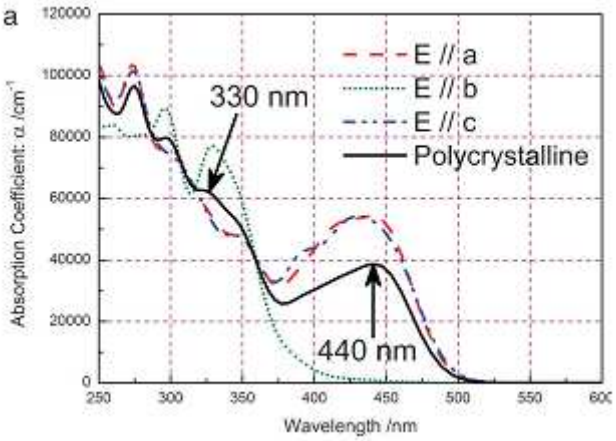

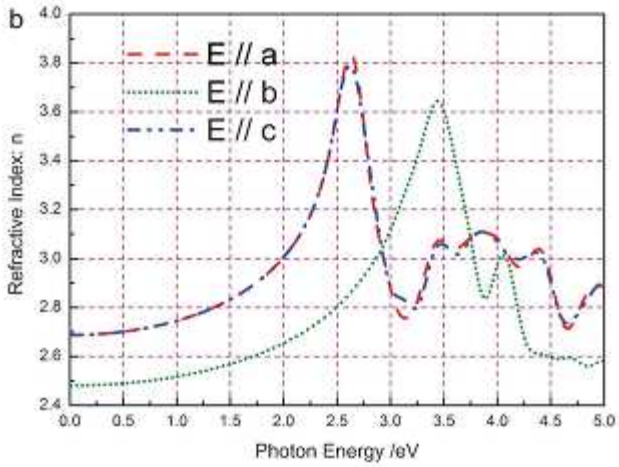

Fig. 14 The absorption coefficient (a) and the refractive index (b) of monoclinic clinobisvanite $BiVO_4$ for different polarization vectors as function of photon energy. Figure taken from [42]

This is the reason of the optical anisotropy.[42] The consequence is that the visible light absorption mainly derives from the photons incident on the a and the c directions. Consequently morphology control of the bismuth vanadate can lead to an enhanced photoactivity by the formation of materials that have exposed the (100) and (001) crystal facets.[44]

Route of synthesis

Different wet routes of synthesis are reported in literature for the preparation of monoclinic bismuth vanadate, among which the solution combustion method,[37, 45, 46] coprecipitation methods followed by hydrothermal synthesis with[34, 47, 48] or without[47, 49, 50] templates, coprecipitation with templates followed by calcination [39, 40, 51], microemulsion-mediated synthesis[52] and the citrate precursor method can be cited.[53-55]

In this work, wet synthesis approaches were used, and in particular the coprecipitation method followed by both hydrothermal treatment and calcination and the citrate precursor method. These synthesis routes are fully described in the Experimental section presented in Chapter 5.1.

3.2 Titanium dioxide (TiO_2)

Crystalline structure

Four different polymorph phases of titanium dioxide are known: anatase (tetragonal), rutile (tetragonal), brookite (orthorhombic) and TiO_2 (B) (monoclinic). Two synthetic phases obtained at high pressure are also reported: TiO_2 (II)(with PbO_2 structure) and TiO_2 (H)(with hollandite structure).[10, 26, 56]

The first three polymorphs are the most common ones and the most largely used in photocatalysis, in particular anatase and rutile. The structure of these three polymorphs can be described in terms of octahedral units, formed by one atom of Ti^{IV} coordinated by six atoms of oxygen. Each structure differs for the distortion of these octahedra and by their assembly pattern. Anatase is built up by the sharing of the vertices forming (001) planes, resulting in a tetragonal structure. Rutile is formed by the sharing of the octahedral edges at (001) planes, giving a tetragonal structure as well, while in brookite the octahedra are united by both edges and corners in an orthorhombic structure. [10, 20, 24]

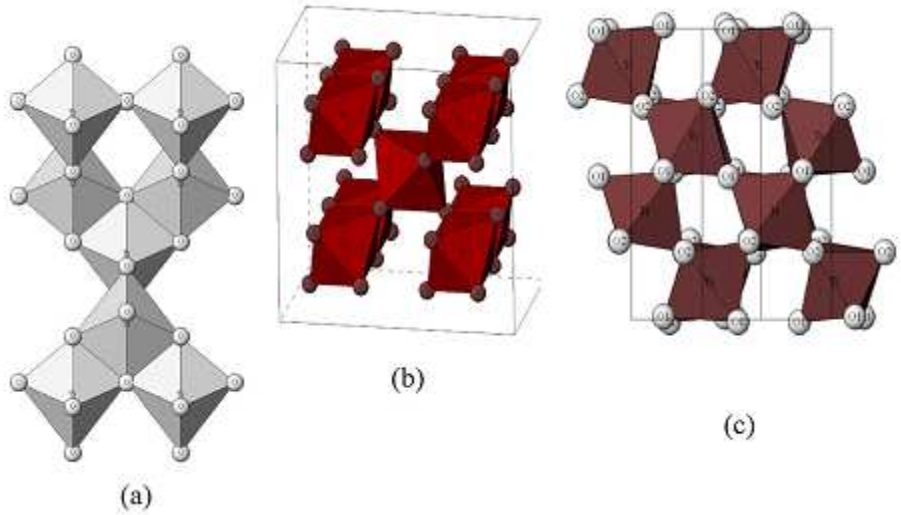

Fig. 15 Crystalline structure of titanium dioxide (a) anatase, (b) rutile, (c) brookite. Figure taken from [24]

The thermodynamically stable polymorph is rutile, that can be easily obtained by heating the brookite and the anatase forms at temperatures above 600°C, but the slight difference in the Gibbs free energy (4-20 kJ/mol) between the three phases suggests that the metastable polymorphs are stable as well under normal pressure and temperature.[10, 56] Studies on the particle size effects have shown that the thermodynamic stability may reverse with the decreasing of the particle dimension, due to surface–energy effects: if the three polymorph phases have the same crystallite size, anatase results the most stable one when dimensions are lower than 11 nm, brookite is the most stable with size ranging between 11 and 35 nm while rutile is the most stable at sizes larger than 35 nm.[10, 26, 57]

Anatase is usually considered the most photoactive phase although in literature this is a point of controversy. Usually, the discrepancies are between the anatase and rutile phases, since some works reported the latter as the most active; several reasons are proposed to explain this variety of results, as the electronic or surface variations.[10, 19-21, 25] Often it is reported that the most active species is a mixture of anatase and rutile, like the benchmark photocatalyst Evonik Aeroxide P25. Among other reasons, this behavior has been attributed to the formation of n-p junctions due to the contact of the crystals of both phases, which improves the charge separation.[20]

Electronic structure

TiO_2 is a typical n-type semiconductor, because of the presence of a small amount of oxygen vacancies, which are compensated by the presence of Ti^{III} centers. The diversity in the lattice structures leads to different electronic densities and to different band structures, giving band gaps of 3.2 eV for anatase, 3.02 eV for rutile and around 3.2 eV for brookite. All these phases absorb in the UV region.[10, 20, 24]

The valence band is mainly formed by the overlapping of the O 2p orbitals, while the lowest part of the conduction band is principally formed by Ti^{IV} 3d orbitals, with symmetry t_2g.[20] The reduction potential at pH 7 of the photogenerated holes is +2.53 V versus the standard hydrogen electrode, while the reduction potential of the conduction band is -0.52 V.[16] The interband transitions in TiO_2 are indirect, but the presence of dopants or the different crystalline size can lead to different type of transitions.[20]

Routes of synthesis

Different methods of preparation of TiO_2 are reported in the literature. They can be roughly divided in wet chemistry and gas phase approaches. The first category includes precipitation methods, solvothermal synthesis, sol-gel methods, microemulsion route, combustion synthesis and electrochemical synthesis.[10]

More common routes belong to the gas phase methods, as chemical vapor deposition (CVD), physical vapor deposition (PVD), spray pirolysis deposition (SPD) or sputtering, and more unusual ones, like molecular beam epitaxy, dynamic ion beam mixing[10]. There are also some solid state syntheses for the production of titania, but these will not be treated here.

In this work TiO_2 has been synthesized by two wet chemistry routes: hydrothermal synthesis and coprecipitation followed by calcination. The detailed description of these two ways of synthesis will be provided in the Experimental section in Chapter 5.1.

4. Results and discussion

4.1 Chemico-physical and structural characterization

In order to achieve a detailed characterization of the samples, different analyses were carried out.
First of all, X-ray diffraction (XRD) analyses were carried out allowing to identify the crystalline phase of the obtained materials. UV-Vis analyses permit to evaluate the light absorption and to calculate the band gap. Information on the surface composition of the samples was gained by X-Ray Photoelectron spectroscopy (XPS), while BET provided an estimation of the specific surface area.
In section 4.2 the photocatalytic activity measurements are reported, a well as the evaluation of the hydroxyl radical production.
In this chapter the samples are labeled as described in the Experimental section. However, in order to permit a more fluent reading of this work, the table below lists all the samples with the corresponding short name.

Sample	Labeling
Hydrothermal $BiVO_4$	$BiVO_4$-ht
Hydrothermal 80% $BiVO_4$-20% w/w TiO_2	80Bi-20Ti-ht
Hydrothermal 50% $BiVO_4$-50% w/w TiO_2	50Bi-50Ti-ht
Hydrothermal 20% $BiVO_4$-80% w/w TiO_2	20Bi-80Ti-ht
Hydrothermal TiO_2	TiO_2-ht
Calcined $BiVO_4$	$BiVO_4$-c
Calcined 80% $BiVO_4$-20% w/w TiO_2	80Bi-20Ti-c
Calcined 50% $BiVO_4$-50% w/w TiO_2	50Bi-50Ti-c
Calcined 20% $BiVO_4$-80% w/w TiO_2	20Bi-80Ti-c
Calcined TiO_2	TiO_2-c
Citrate $BiVO_4$	$BiVO_4$-ct

Tab. 1 Labeling of the samples

4.1.1 XRD

Hydrothermal products

The figure below reports the diffractograms of the hydrothermal products plotted with normalized intensity.

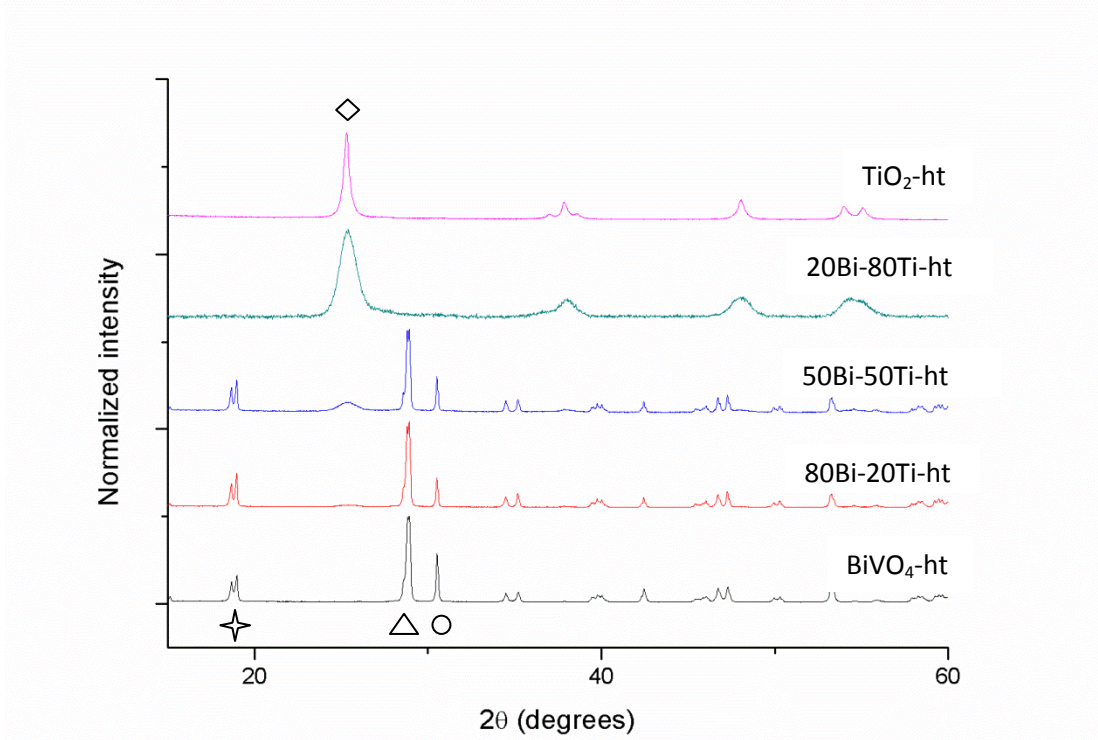

Fig. 16 XRD diffractograms (with normalized intensity) of $BiVO_4$, TiO_2 and composites obtained through hydrothermal synthesis. The four point star, the triangle and the circle indicate the main reflections of monoclinic $BiVO_4$, the square indicates the main reflection of anatase.

For the identification, two powder diffraction files (PDF) were used: ICSD PDF file 00-014-0688 for monoclinic scheelite and ICSD PDF file 01-083-2243 for anatase.

As it can be seen from Fig. 16, the main structure for $BiVO_4$ (and for the composites with the 80% and 50% of it) is the monoclinic scheelite, while the patterns of 20% $BiVO_4$-80% TiO_2 and TiO_2 reveal anatase as the main phase. There are no diffraction reflections generated by impurities or by other phases, and also in the composites the main phases (i.e. monoclinic scheelite and anatase) are present. This shows that the hydrothermal treatment, carried out as described in the Experimental section (Chapter 5.1), is suitable for the production of monoclinic scheelite and anatase, both as pure materials (as reported in previously works[47]) and as heterostructures.

In Fig. 17 the same diffractograms are reported, using not normalized intensity, in order to evaluate the increasing (or decreasing) of the main phase reflections, that are 28.8° (indicated with a triangle), 30.5° (indicated with a circle) and the ones at 18.8° and 18.9° (indicated with a four point star) for monoclinic bismuth vanadate and 25.3° (indicated with a square) for anatase.

In Fig. 17 it can be observed that the monoclinic phase decreases when the amount in titania is increased. In fact there is a reduction of the most intense reflection at 28.8°, (besides the reduction of other characteristic reflections, like the one at 30.5° or the ones at 18.8° and 18.9°), while the reflections of anatase (especially the most intense one at 25.3°) grow until it becomes the only detectable phase in 20Bi-80Ti-ht composite.

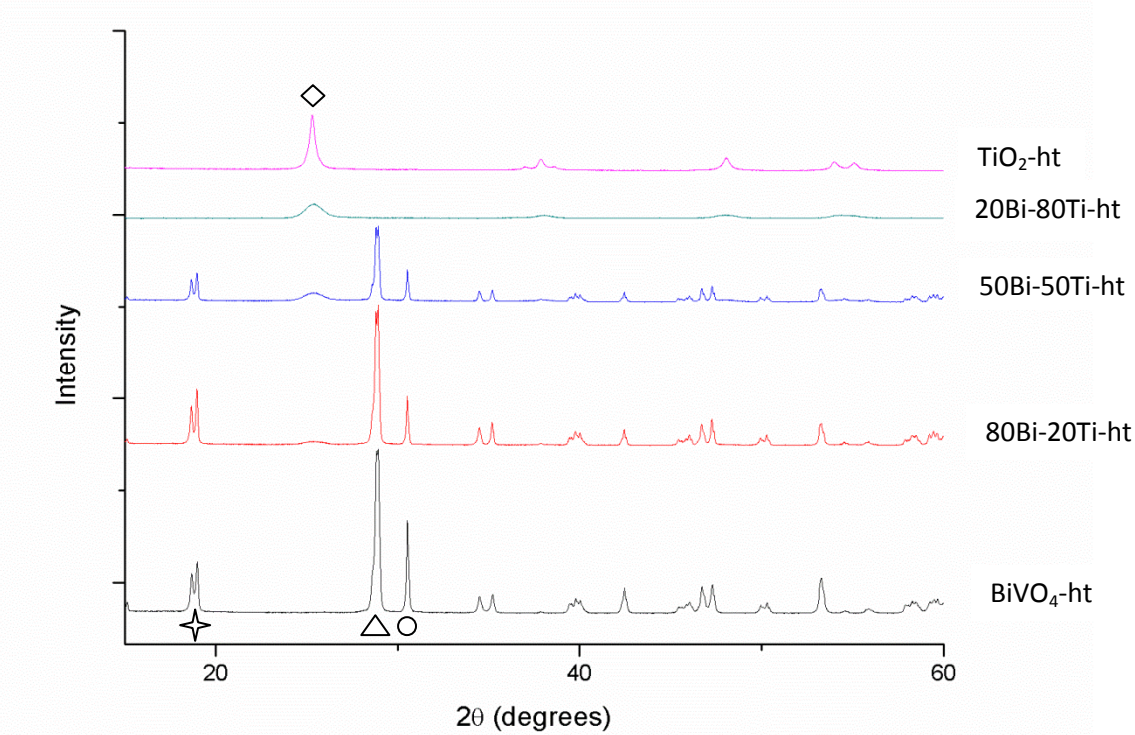

Fig. 17 XRD diffractograms of $BiVO_4$, TiO_2 and composites obtained through hydrothermal synthesis. The four point star, the triangle and the circle indicate the main reflections of monoclinic $BiVO_4$, the square indicates the main reflection of anatase.

	Sample	**$BiVO_4$-ht**	**80Bi-20Ti-ht**	**50Bi-50Ti-ht**	**20Bi-80Ti-ht**	**TiO_2-ht**
Monoclinic scheelite	**a (Å)**	5.196	5.196	5.195	-	-
	b (Å)	5.097	5.096	5.095	-	-
	c (Å)	11.707	11.702	11.702	-	-
	α (degrees)	90.035	89.953	89.9	-	-
	β (degrees)	90.054	90.046	89.98	-	-
	γ (degrees)	90.280	90.342	90.277	-	-
	Crystallite size (nm)	55	95	71	-	-
Anatase	**a (Å)**	-	3.726	3.739	3.791	3.787
	b (Å)	-	3.726	3.739	3.791	3.787
	c (Å)	-	9.625	9.416	9.467	9.498
	α (degrees)	-	90	90	90	90
	β (degrees)	-	90	90	90	90
	γ (degrees)	-	90	90	90	90
	Crystallite size (nm)	-	10	11	9	26

Tab. 2 Cell parameters and average dimension of crystallites of hydrothermal products

In Tab. 2 cell parameters, calculated as reported in Chapter 6.1, are listed, and these values confirm the cell structure of the compounds, that is monoclinic for $BiVO_4$ ($a \neq b \neq c$, $\alpha=\beta=90°$ $\gamma \neq 90°$)[58] and the tetragonal phase for anatase ($a=b \neq c$, $\alpha=\beta=\gamma=90°$)[58]. The bismuth vanadate structure is a little bit distorted, α and β not

exactly equal to 90°. The average dimensions of the crystallites, calculated with the Scherrer equation (Chapter 6.1), are also reported. The crystallite sizes of the monoclinic structure result bigger than the ones of the tetragonal anatase.

Calcined products

In Fig. 18 the XRD patterns (with normalized intensities) of the calcined composites and pure phases are reported.

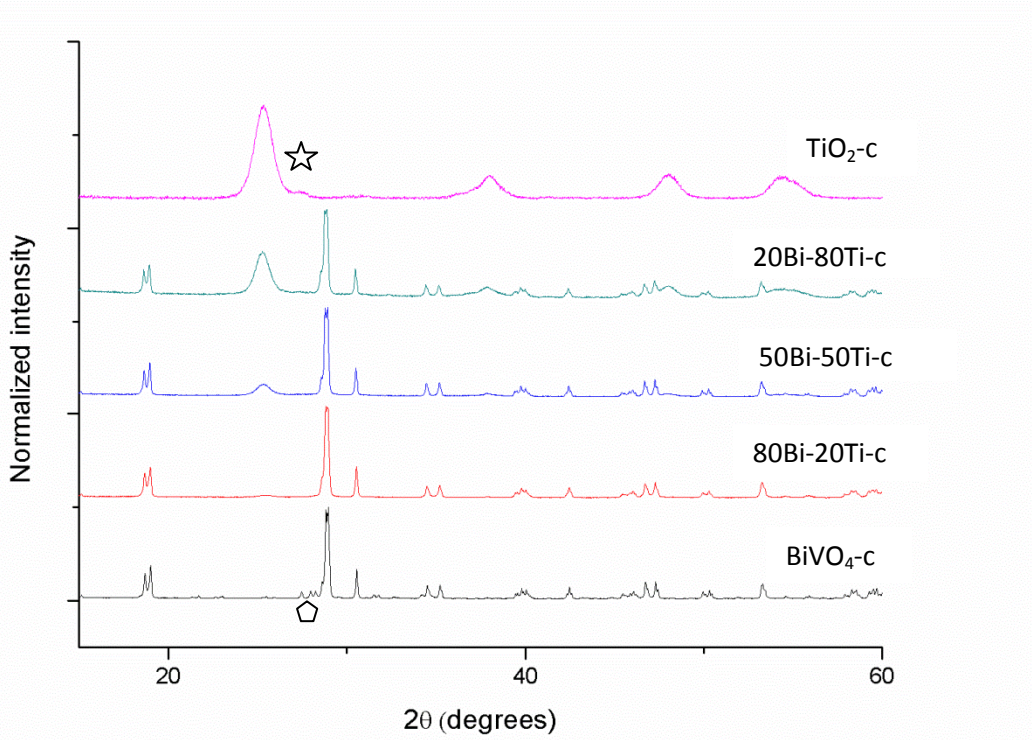

Fig. 18 XRD diffractograms (with normalized intensity) of $BiVO_4$, TiO_2 and composites obtained through thermal synthesis. The five point star indicates the rutile reflections, while the pentagon indicate the unidentified reflections in monoclinic $BiVO_4$.

In the calcined composites the phase of bismuth vanadate is the monoclinic one, while the phase for the titanium dioxide is the anatase one. The pure materials present some minor reflections that do not belong neither to anatase nor to clinobisvanite patterns.

The $BiVO_4$-c presents three reflections at 27.4°, 27.9° and 28.2° (indicated with a pentagon in Fig. 18) that derives neither from monoclinic, nor from tetragonal (ICSD PDF file 00-001-0359) nor from zircon type (ICSD PDF file 00-012-0293) polymorph. In TiO_2-c also a low amount of rutile structure is present, which is revealed by the small reflection at 27.5°, indicated by a five point star in Fig. 18 (ICSD PDF file 00-001-0562).

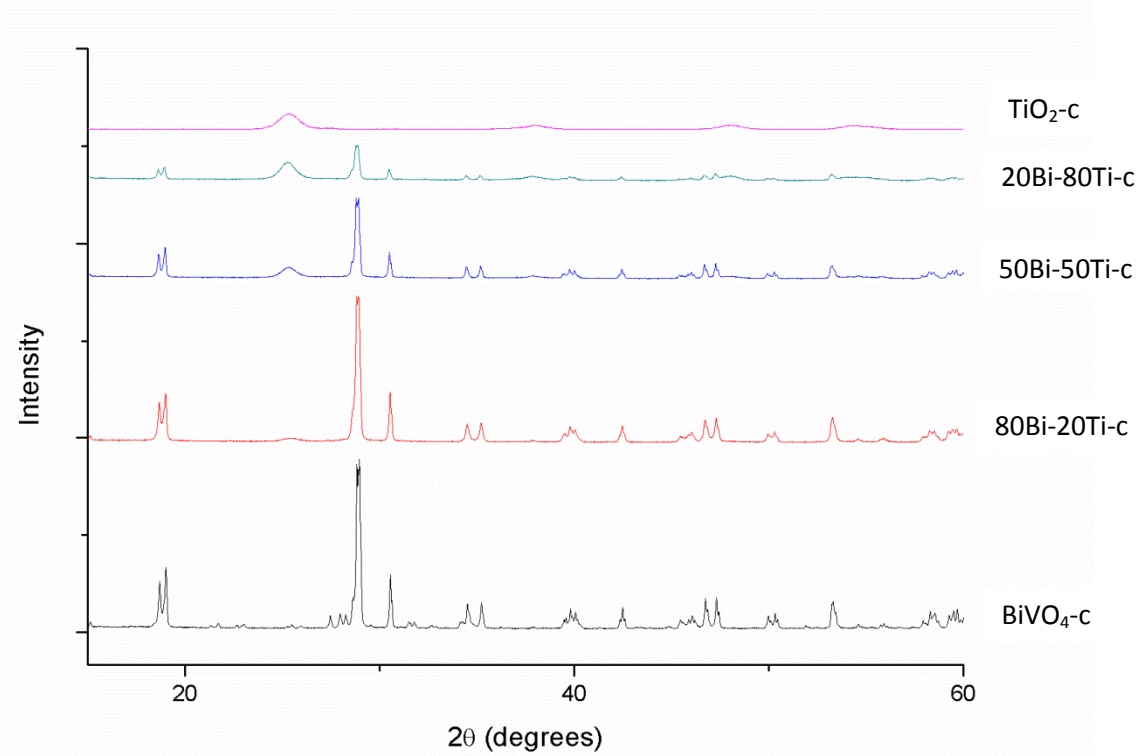

Fig. 19 XRD diffractograms of $BiVO_4$, TiO_2 and composites obtained through thermal synthesis

	Sample	**$BiVO_4$-c**	**80Bi-20Ti-c**	**50Bi-50Ti-c**	**20Bi-80Ti-c**	**TiO_2-c**
Monoclinic scheelite	**a (Å)**	5.190	5.197	5.198	5.197	-
	b (Å)	5.064	5.094	5.094	5.105	-
	c (Å)	11.759	11.702	11.704	11.729	-
	α (degrees)	88.776	89.9	89.885	90.087	-
	β (degrees)	91.438	89.98	90.081	90.020	-
	γ (degrees)	89.830	90.383	90.260	90.306	-
	Crystallite size (nm)	80	81	84	62	-
Anatase	**a (Å)**	-	3.693	3.741	3.812	3.788
	b (Å)	-	3.693	3.741	3.812	3.788
	c (Å)	-	9.426	9.419	9.602	9.476
	α (degrees)	-	90	90	90	90
	β (degrees)	-	90	90	90	90
	γ (degrees)	-	90	90	90	90
	Crystallite size (nm)	-	60	12	10	76

Tab. 3 Cell parameters and average dimension of crystallites of thermal products

In Fig. 19 it is possible to see the typical reflections of anatase becoming stronger accordingly with the higher amount of titania in the composites, and the consequent decreasing of the bismuth vanadate ones. In Tab. 3 the parameters of the unit cell, as well the crystallite sizes (calculated with the Scherrer equation), are reported. The cell parameters are typical of a monoclinic cell (for $BiVO_4$) and of a tetragonal cell (for TiO_2). In addition the parameters obtained for the calcined samples are very similar to the one obtained for the samples that underwent

hydrothermal treatment. Also with the thermal route of production, the monoclinic structure is a little bit distorted, with the angles α and β being not exactly 90°.
The average dimensions of the crystallites are, instead, quite different if compared with the hydrothermal compounds. In general, an increase of the crystallite size is observed in the high temperature treated samples. This is expected since, in order to minimize the surface free energy of the system, the crystallites undergo sintering and coalescence phenomena.[59-62]
The effect of the temperature is more evident in the anatase crystallites, especially for the pure titania and for the composite 80Bi-20Ti-c.

Citrate precursors synthesis

In Fig. 20 the XRD pattern of the bismuth vanadate obtained by using citrate route is reported.

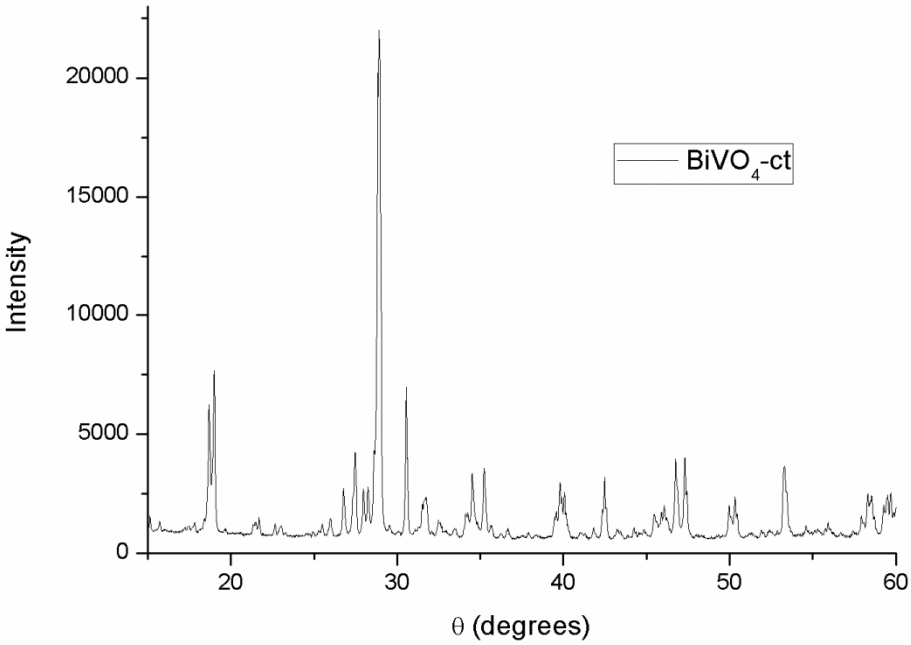

Fig. 20 XRD pattern of $BiVO_4$-ct

The pattern shows the presence of different phases: some of the reflections can be ascribed to bismuth vanadate polymorphs (tetragonal scheelite and zircon type structure), whereas some other were not identified. The calculation of the cell parameters is not useful because of the presence of many phases. For this reason this route was not further explored.

4.1.2 UV-Vis diffuse reflectance spectra

Diffuse reflectance UV-Vis spectra were recorded for all the samples, in order to obtain the absorption properties of the catalysts and to estimate the value of the semiconductors band gap. The spectra are reported in Fig. 21.

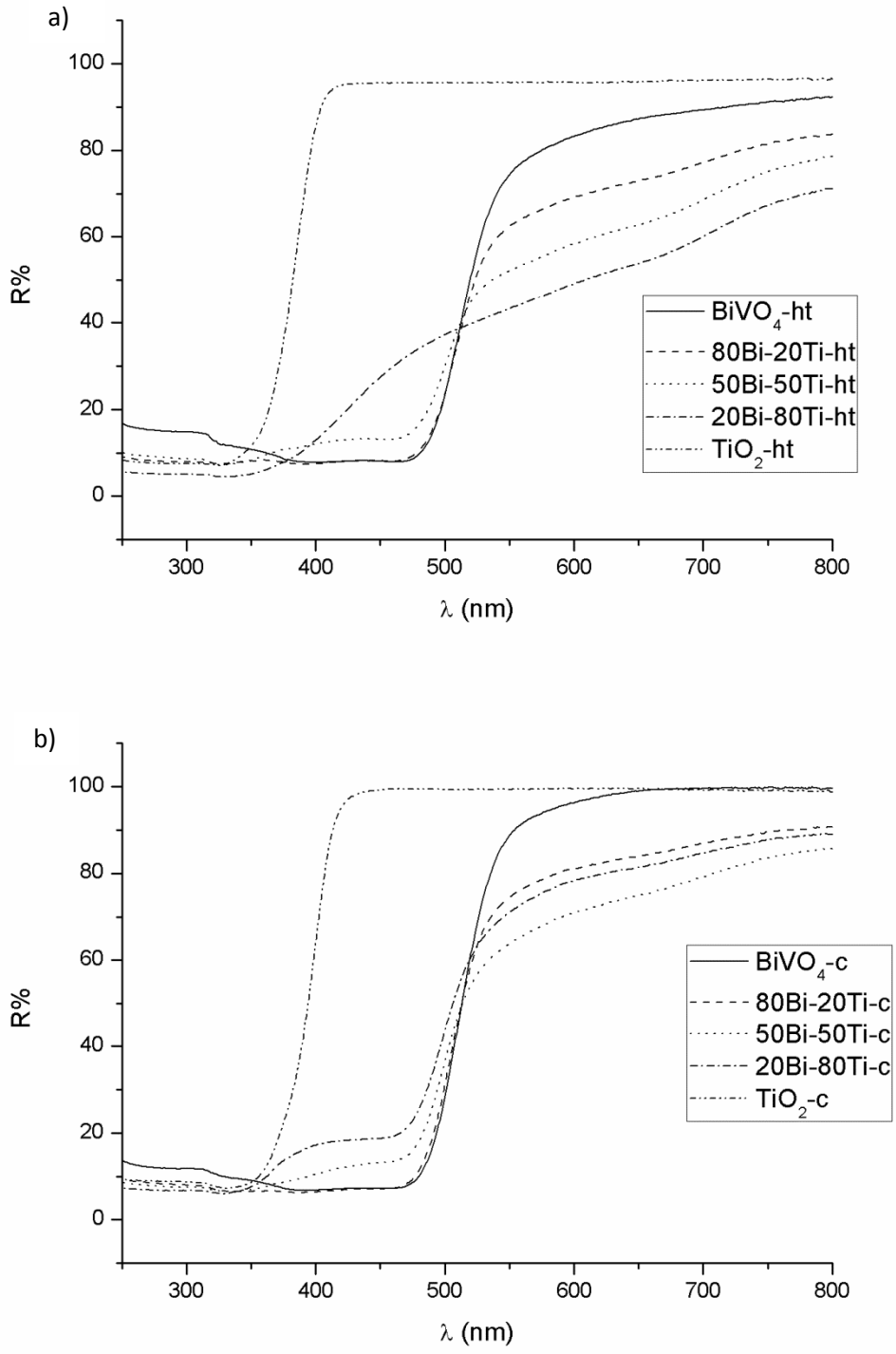

Fig. 21 Diffuse reflectance spectra of a) hydrothermal products and b) calcined products.

The absorbance of the composites in the visible region increases as the amount of bismuth vanadate is increased, as reported also in other works.[31] The change in

light absorption can be inferred even from the colors of the various compounds. Bismuth vanadate has a strong yellow color; adding titania (which is white) the tone of the yellow changes in two different manners, depending on the used synthesis route, as shown in Fig. 22. In the samples prepared by thermal method the color becomes lighter with the increasing amount of titania, but it still remains on the yellow shade. With the hydrothermal route the color becomes lighter, but it turns on a brown tone.

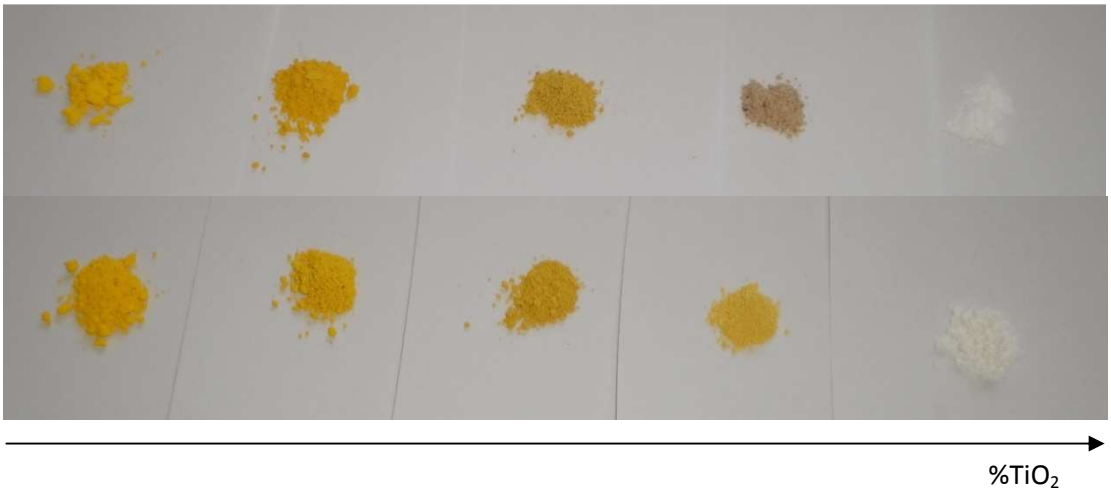

Fig. 22 Color change in the products. The upper row is formed by the hydrothermal compounds, the lower by the calcined compounds, with increasing amount of titania from the left to right.

This behavior is mostly evident in the sample 20Bi-80Ti-ht. This can be likely due to the low amount of $BiVO_4$ in the composite, as shown by XRD analysis, that can not give the typical yellow color as the other compounds.
From the diffuse reflectance spectra an approximate value of the band gap can be calculated.
The absorbance coefficient α is defined as:[63]

$$\alpha = -\ln R = \frac{[B(h\upsilon - E_g)]^n}{h\upsilon}$$

where R is the reflectance intensity, B an absorption constant, hν is the energy of the radiation, E_g is the band gap energy and n is a parameter equal to ½ for direct semiconductors, and equal to 2 for indirect semiconductor. After some rearrangements, the formula results in:

$$(\alpha h\upsilon)^{1/n} = Bh\upsilon - BE_g$$

so that when $(\alpha h\nu)^{1/n}$ is set equal to 0, hν takes the value of the band gap energy
If $(\alpha h\nu)^{1/n}$ is plotted versus the energy (hν) a straight line is obtained in the absorption edge, and the extrapolation of this line to $(\alpha h\nu)^{1/n}=0$ gives the E_g value in the abscissa axis. This type of diagram is called Tauc plot. In Fig. 23 a Tauc plot is reported as example.

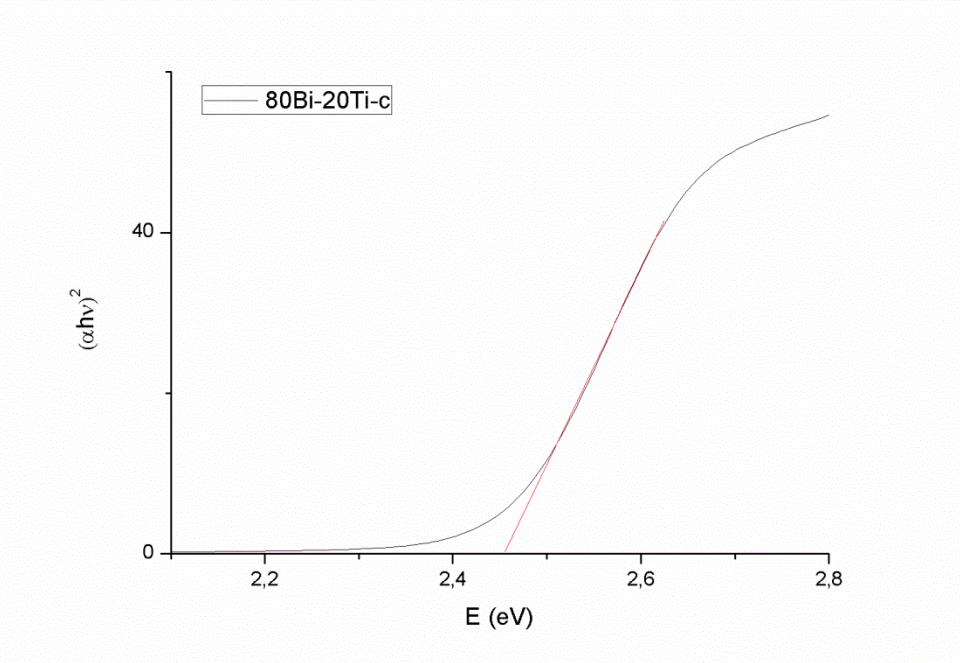

Fig. 23 Tauc plot of the composite 80Bi-20Ti-c.

From this formula the indirect band gap of titania was calculated, while for $BiVO_4$, both direct and indirect band gaps were calculated. For the composites the graphs permitted to calculate only the direct and indirect band gap of bismuth vanadate. The results are listed in Tab. 4.

Sample	Direct band gap energy (eV)	Indirect band gap energy (eV)
$BiVO_4$-c	2.44	2.23
$BiVO_4$-ct	2.42	2.21
$BiVO_4$-ht	2.42	2.17
80Bi-20Ti-c	2.46	2.21
80Bi-20Ti-ht	2.42	2.15
50Bi-50Ti-c	2.44	2.16
50Bi-50Ti-ht	2.41	2.07
20Bi-80Ti-c	2.44	2.15
20Bi-80Ti-ht	2.42	1.75
TiO_2-c	-	2.92
TiO_2ht	-	2.98

Tab. 4 Band gap energies of all the compounds

The band gap values obtained with n=1/2 (direct band gap) are really close to the one reported in literature[43], while the values obtained for titania as an indirect band gap are slightly smaller than the value reported in literature.[10, 24]

4.1.3 BET analysis

BET analysis permits an evaluation of the specific surface area of the samples. The results are listed in the Tab. 5.

Sample	BET specific surface area (m^2/g)
$BiVO_4$-ht	1.4
80Bi-20Ti-ht	41.4
50Bi-50Ti-ht	98.2
20Bi-80Ti-ht	178.4
TiO_2-ht	46.4
$BiVO_4$-c	1.2
80Bi-20Ti-c	13.0
50Bi-50Ti-c	40.9
20Bi-80Ti-c	61.3
TiO_2-c	62.9
$BiVO_4$-ct	0.5

Tab. 5 BET specific surface areas

$BiVO_4$ (obtained both by thermal and hydrothermal treatment) has a low specific surface area, if compared with the one of TiO_2. Consequently, in the composites the specific surface area increase as the amount of titania increases. This trend is linear in the calcined samples, *i.e.* the surface area increases as the amount of bismuth vanadate decreases, reaching the maximum value for TiO_2-c. In the samples prepared by hydrothermal route, instead, the behavior is different. In fact the specific surface area of the composites increases as the quantity of TiO_2 increases, but the area is much higher in the 50Bi-50Ti-ht and 20Bi-80Ti-ht than in TiO_2-ht. This trend can be visually represented in the graphs reported in Fig. 24

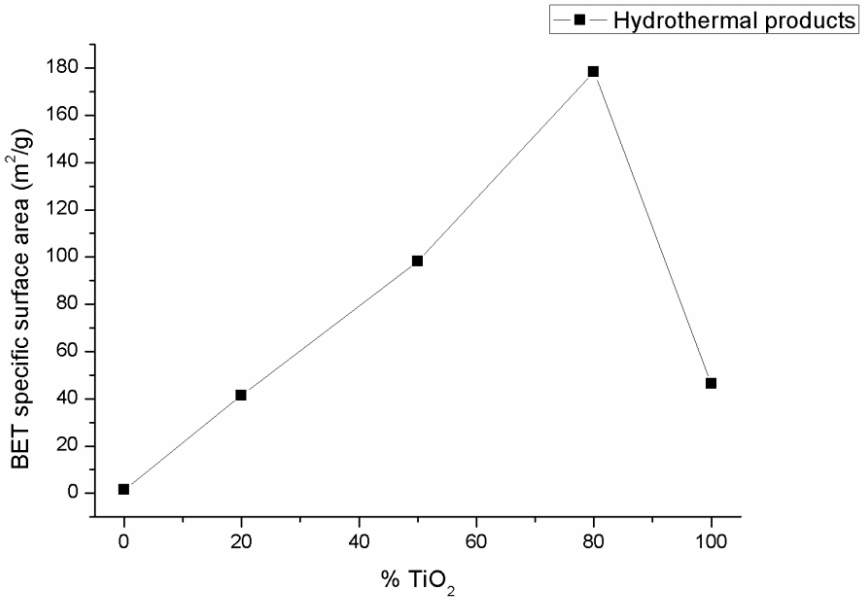

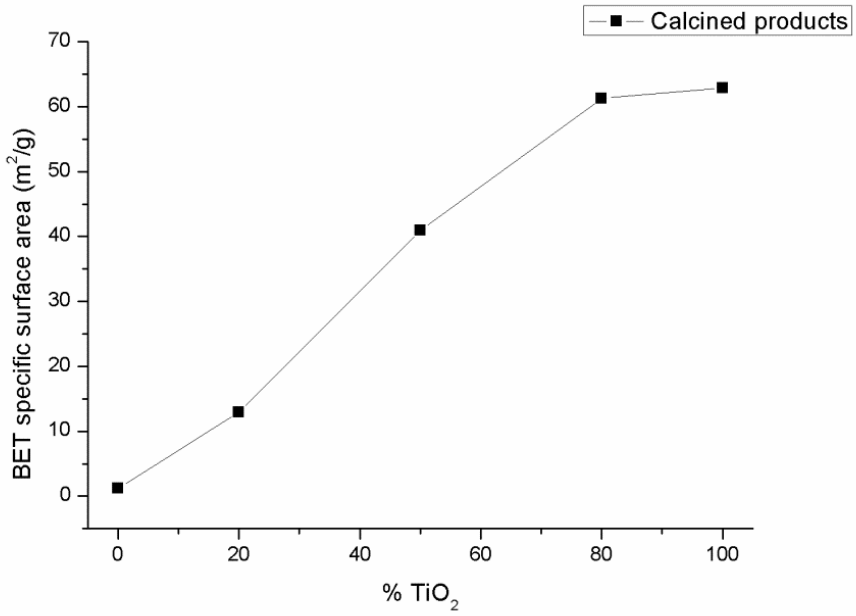

Fig. 24 BET specific surface area vs amount of TiO_2 for hydrothermal (above) and calcined (below) products.

As expected, the values of specific surface area are higher for the samples obtained through hydrothermal treatment than through calcination. This is due to the relatively high temperature used in the latter synthesis route, that favors coalescence and sintering phenomena.[59] But the specific area of the two samples of titania does not follow this trend: TiO_2-c has bigger surface area than TiO_2-ht. This behavior cannot be ascribed to the crystallites dimension, since the former has bigger crystallite than the latter, as revealed from XRD measurements. The explanation cannot be neither the formation of a certain grade of porosity in the calcined sample since, at high temperature, the collapse of porosity is a phenomenon that occurs together with coalescence. A possible explanation could be the presence of other substances on the catalyst surface, that inhibit the adsorption of nitrogen during the measurements. This presence could due to the precursors of the catalysts, that were not well removed during the hydrothermal treatment as during the thermal treatment. In order to exclude the presence of residues from the precursors, FT-IR spectra were performed. They do not present any peak that can be ascribed to organic molecules deriving from the synthetic precursors, thus confirming the expected oxide composition.

4.1.4 XPS

In order to obtain further information on surface compositions and chemical environments, as well as a quantitative evaluation of the atomic ratios between the surface components of the obtained samples, X-Ray photoelectron spectroscopy (XPS) was employed.

In all samples, the calculated amount of carbon and oxygen (Tab.6) is higher than expected; this is due to the surface contamination of the samples. Furthermore, a not trivial amount of nitrogen was detected on the surface; this presence can be explained by the above mentioned reasons. This result reveals the necessity of an improvement of the purification protocol.

As it can be seen in Tab. 6, the Bi:V atomic ratios obtained from the quantitative analyses are in all cases in good agreement with what was predicted (i.e. Bi:V=1:1). By contrast, the Ti/Bi atomic ratios in samples 80Bi-20Ti and 50Bi-50Ti (both in the case of composites obtained through hydrothermal and thermal synthesis) are considerably higher than the nominal stoichiometric ratio. This titanium enrichment can be likely ascribed to a surface segregation of titania on the composite, or to the formation of core-shell heterostructures. At this regard, TEM measurements would be helpful to clarify the actual nature of the obtained composites.

The reason why this enrichment was not observed in the case of the composites featuring the highest amount of titania is however not easy to rationalize.

Sample	%C	%N	%O	%Ti	%V	%Bi	Theoretical Ti/Bi atomic ratio	Experimental Ti/Bi atomic ratio
$BiVO_4$-ht	61.5	2.3	26.6	-	4.2	5.4		
80Bi-20Ti-ht	31.2	2.4	45.5	14.0	3.4	3.5	1	4
50Bi-50Ti-ht	32.6	1.7	46.6	14.9	2.1	2.1	4	7
20Bi-80Ti-ht	38.9	1.3	43	14.0	1.7	1.1	16	14
TiO_2-ht	21.4	-	57.3	21.3	-	-		
$BiVO_4$-c	44.2	4.4	37.0		6.4	8.0		
80Bi-20Ti-c	46.5	5.8	33.3	8.2	3.0	3.2	1	2.5
50Bi-50Ti-c	32.2	2.6	45.9	14.3	2.7	2.4	4	6
20Bi-80Ti-c	35.5	0.9	45.8	15	1.8	1.1	16	15
TiO_2-c	19.2	0.1	51.4	18.0	-	-		

Tab. 6 Atomic percentages as determined by XPS quantitative analysis

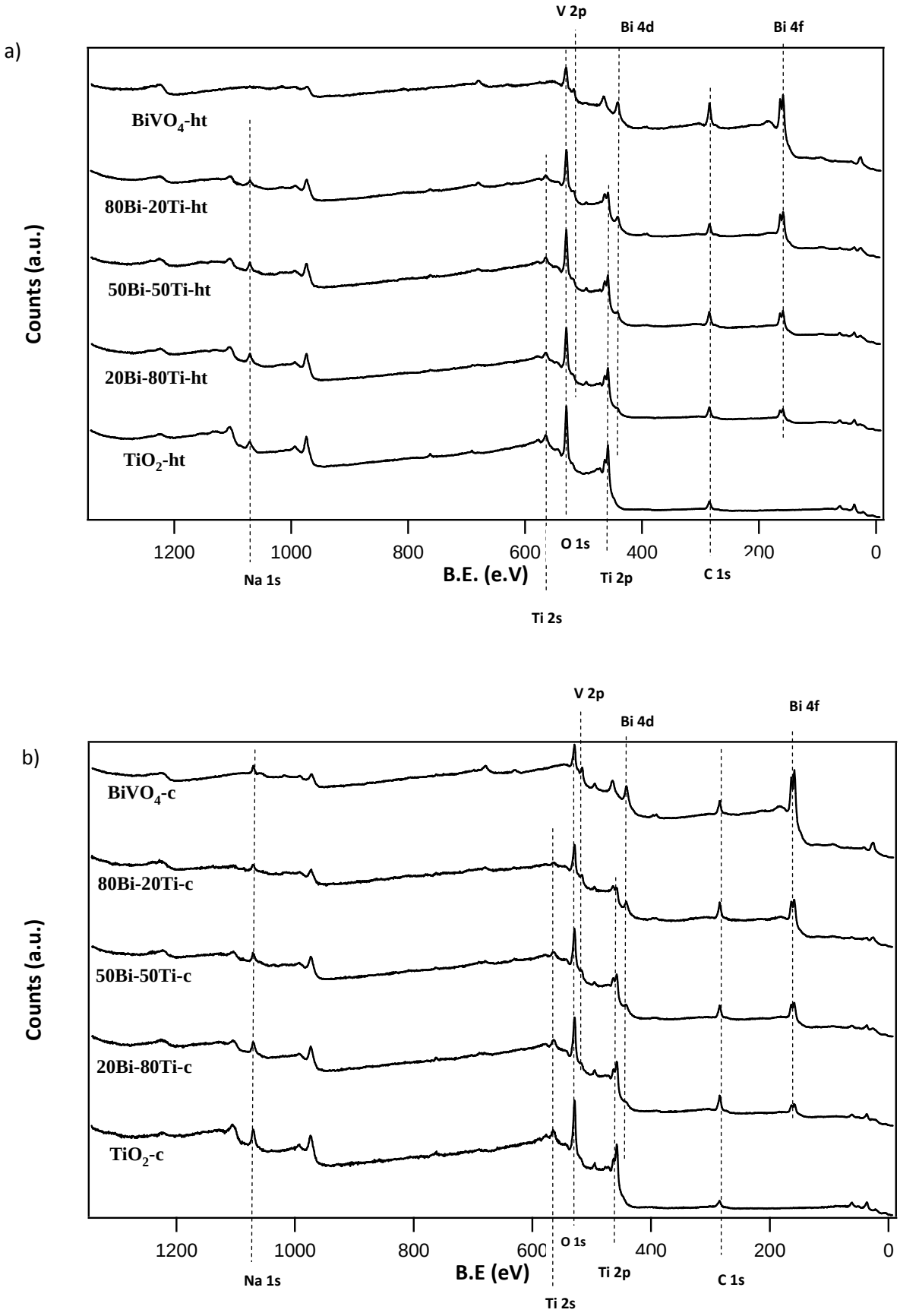

Fig. 25 XPS spectra of a) hydrothermal and b) thermal products, reported with the B.E. corrected for charge effects

Sample	Bi $4f_{7/2}$	Bi $4f_{5/2}$	C 1s	Ti $2p_{3/2}$	Ti $2p_{1/2}$	V $2p_{3/2}$	V $2p_{1/2}$	O 1s
$BiVO_4$-ht	158.5	163.9	284.6	-	-	516.2	523.5	529.3
80Bi-20Ti-ht	158.5	163.8	284.6	458.0	463.8	516.1	523.2	529.3
50Bi-50Ti-ht	158.7	164.1	284.6	458.2	464.1	516.5	523.5	529.3
20Bi-80Ti-ht	158.8	164.1	284.6	458.1	463.9	516.9	523.2	529.4
TiO_2-ht	-	-	284.6	458.1	463.9	-	-	529.3
$BiVO_4$-c	158.3	163.6	284.6	-	-	515.9	523.4	529.0
80Bi-20Ti-c	158.5	163.9	284.6	458.0	463.8	516.4	523.4	529.3
50Bi-50Ti-c	158.7	164.0	284.6	458.2	464.0	516.4	523.5	529.3
20Bi-80Ti-c	158.6	164.0	284.6	458.2	464.0	516.4	523.1	529.6
TiO_2-c	-	-	284.6	457.8	463.4	-	-	528.8

Tab. 7 BE values of the main peaks. Binding energies are corrected for charging effects.

In the survey spectra (Fig 25) all elements of interest (Bi, V, Ti, C and O, highlighted with dashed lines) are visible. A signal at about 1071 eV is present in the spectra of both the hydrothermal (excluding $BiVO_4$-ht) and the thermal compounds. This peak is relative to the 1s transition of sodium, and its presence is due to the precursors (NaOH) used during the syntheses.

As far as the chemical environment and oxidation states are concerned, related information was gained by high resolution selected spectra of the species of interest, allowing determination of the binding energies (BE), reported in Tab. 7. The experimental values were corrected for the charging effects by assigning the BE value of 284.6 eV to the C 1s line (relative to adventitious carbon).[64]

Concerning bismuth, the positions of the Bi $4f_{5/2}$ and Bi $4f_{7/2}$ peaks (163.6-164.1 eV and 158.3-158.7 eV, respectively) indicate that this element is present as $Bi^{(II)}$. The binding energy values are typical for bismuth in $BiVO_4$.[34]

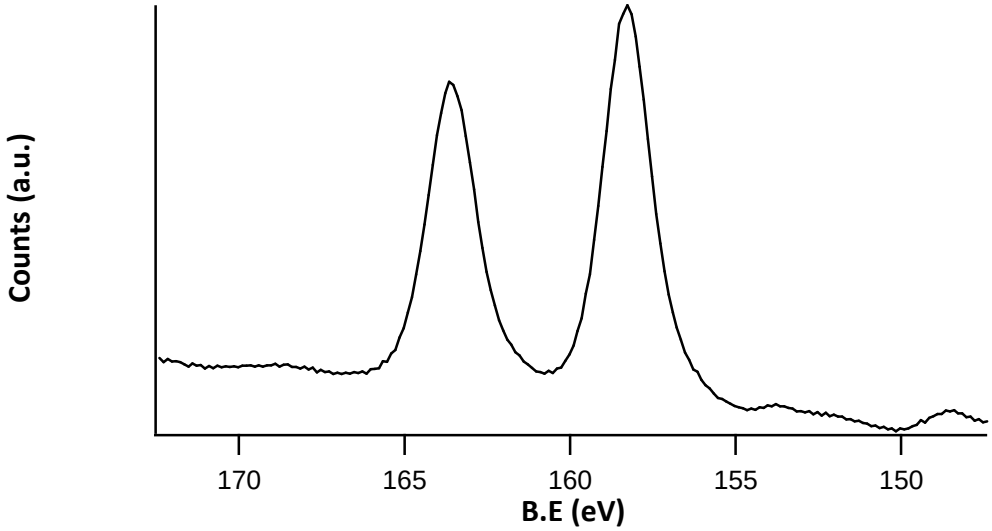

Fig. 26 Bi 4f peak of $BiVO_4$-c

The $2p_{3/2}$ and $2p_{1/2}$ components of the vanadium 2p peak (Fig. 27), located respectively at 515.9-516.9 eV and at 523.1-523.5 eV, display also binding energy values typical of $V^{(V)}$ as reported by other authors.[34, 48, 50, 65]

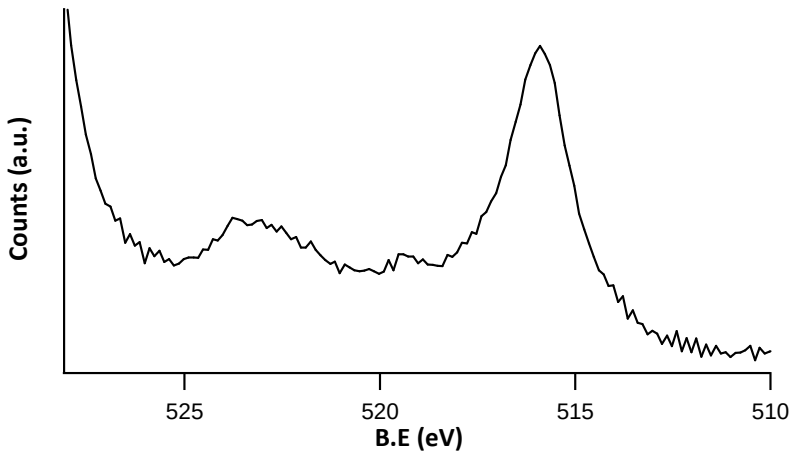

Fig. 27 V 2p peaks of BiVO4-c

The signal of O 1s is obviously present in all the samples, but in $BiVO_4$-ht, it presents a shoulder, as shown in Fig. 28. This asymmetric peak indicates that oxygen is present on the surface not only as lattice oxygen, but also under other species, which could be hydroxyl oxygen or adsorbed oxygen.[34, 50, 65]

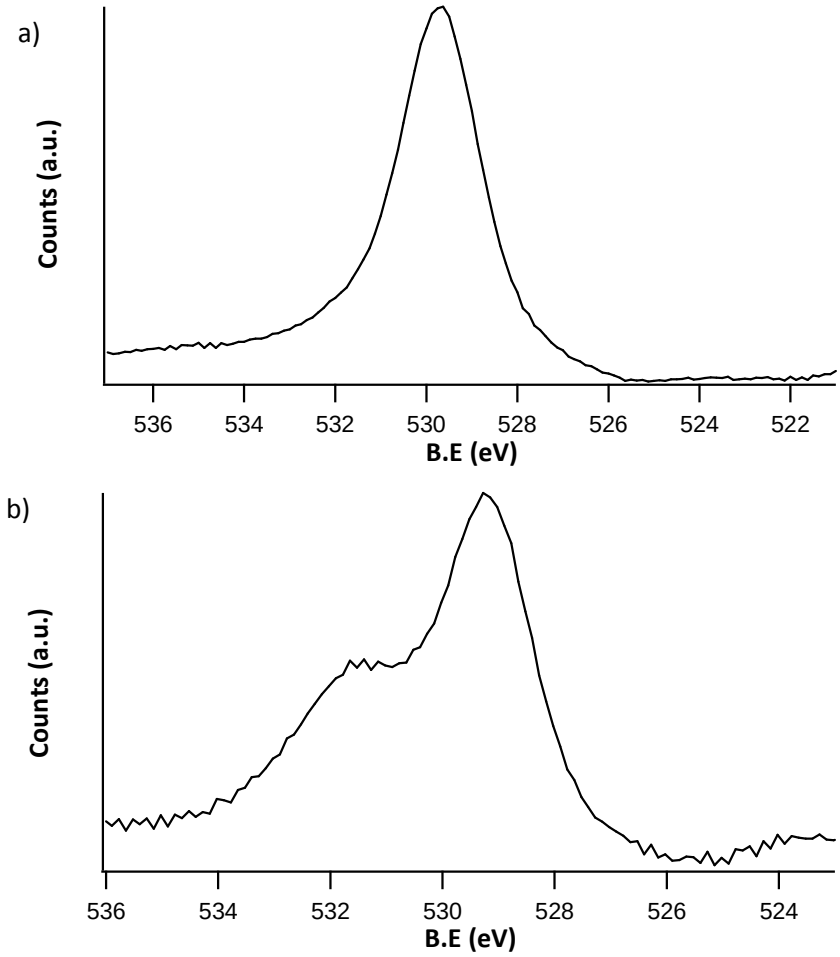

Fig. 28 O 1s peak of 20Bi-80Ti-c (a), and $BiVO_4$-ht (b).

The Ti $2p_{1/2}$ peak (at 463.4-464.1 eV) and Ti $2p_{3/2}$ peak (at 457.8-458.2 eV), have typical binding energies of Ti^{IV} in titania as reported by other authors for anatase.[66]

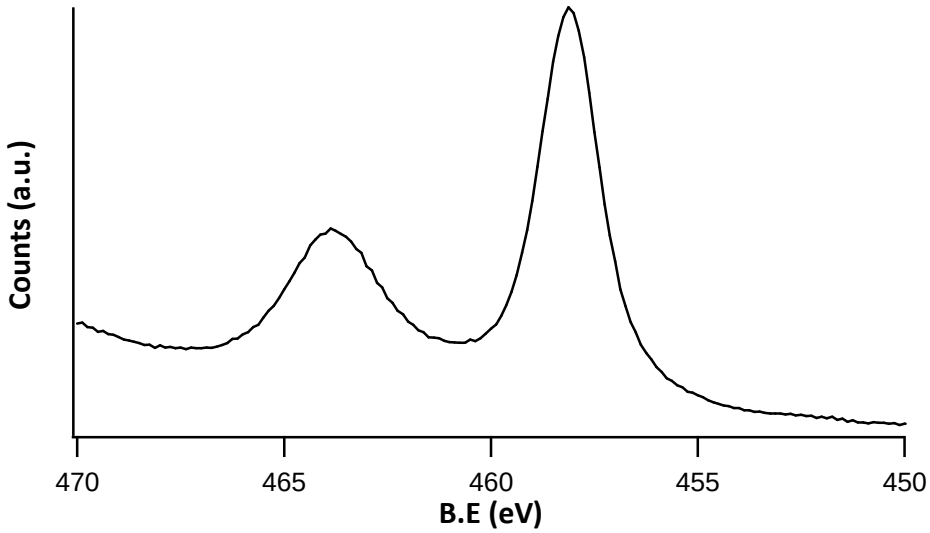

Fig. 29 Ti 2p peak of TiO_2-ht

4.2 Photocatalytic activity

4.2.1 Hydrothermal products

The photocatalytic activity was evaluated observing the degradation of gaseous isopropanol under irradiation with daylight lamps. The changes in concentration of isopropanol were detected by using a GC-MS, as described in the Experimental section.

Gas phase reaction

The degradation of isopropanol is a first-order kinetics reaction; this means that if the natural logarithm of the initial concentration divided by concentration is plotted against time a straight line should be obtained.[67, 68]
For the generic first order kinetics reaction

$$\mathrm{A} + \mathrm{B} \rightarrow \mathrm{C} + \mathrm{D}$$

The reaction rate is expressed as:

$$\mathrm{r} = -\frac{d\mathrm{A}}{d\mathrm{t}} = \mathrm{kA}$$

And the equation is easily solved, obtaining the relationship between the logarithm of concentration and the time.

$$-\frac{d\mathrm{A}}{\mathrm{A}} = \mathrm{k}d\mathrm{t}$$

$$\ln\left(\frac{\mathrm{A}_0}{\mathrm{A}}\right) = \mathrm{kt}$$

The $\ln(C_0/C)$ against time is reported in Fig. 30, and in Tab. 8 the rate constants obtained by the linear fitting of the curves are reported.

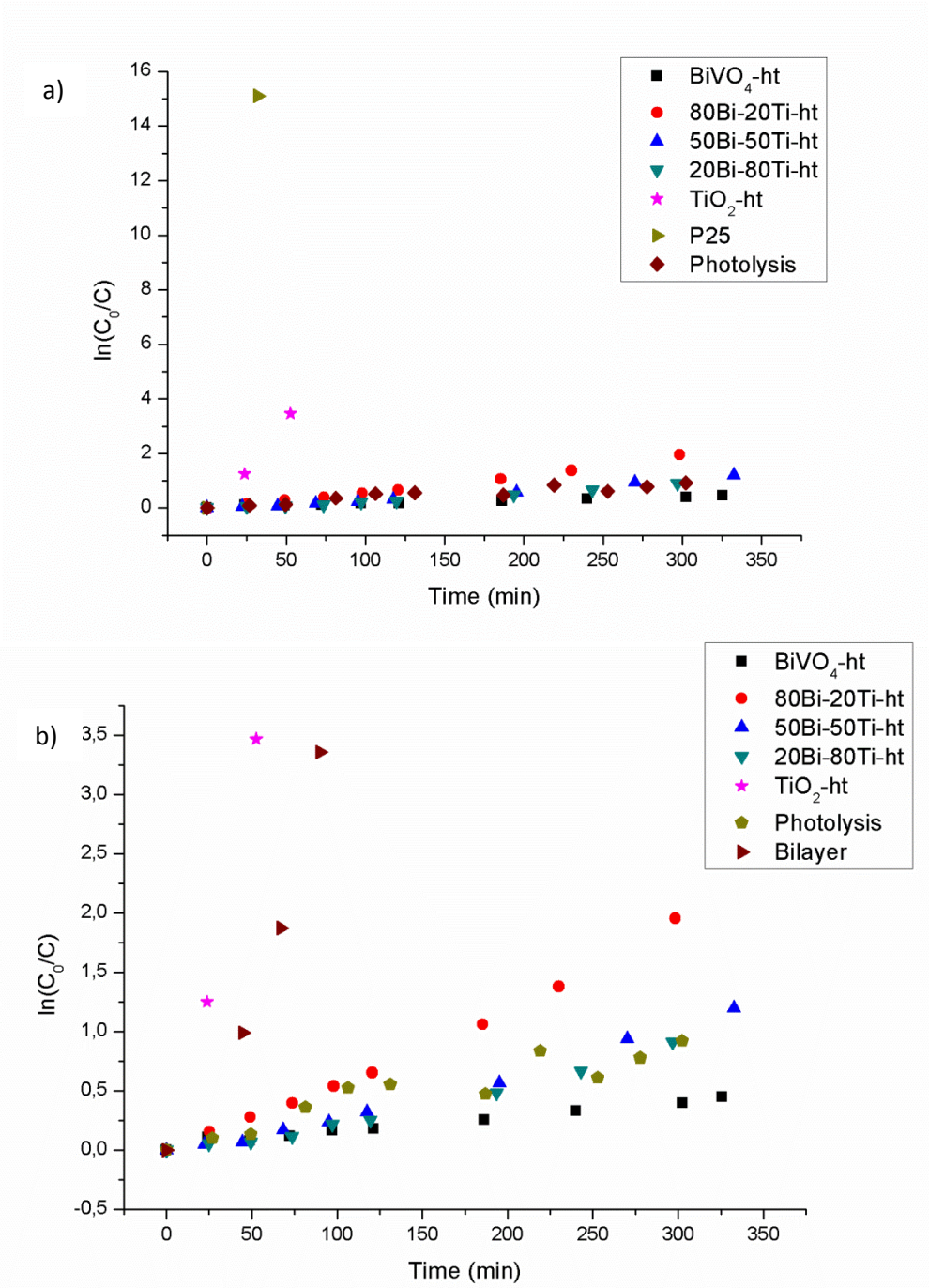

Fig. 30 a) Rate curves of all the hydrothermal compounds toward the degradation of isopropanol. b) Rate curves of the hydrothermal products and the bilayer without P25.

Sample	K (min^{-1})
BiVO4-ht	1.2E-3
80Bi-20Ti-ht	7.8E-3
50Bi-50Ti-ht	3.6E-3
20Bi-80Ti-ht	3.0E-3
TiO2-ht	6.6E-2
P25	0.47
Photolysis	2.7E-3
Bilayer	6.9E-3

Tab. 8 Rate constant of the degradation of isopropanol by hydrothermal products. P25 is a commercial reference, the bilayer is formed by the deposition of a $BiVO_4$-ht layer over a TiO_2-ht layer.

Hydroxyl radical formation

The formation of hydroxiterephtalic acid (HTPA) through hydroxyl radical attack of terephtalic acid (TPA) was followed using a fluorimeter, as reported in the Experimental Section. In Fig. 31 the results are reported. In the Tab. 9 the rate constants are listed.

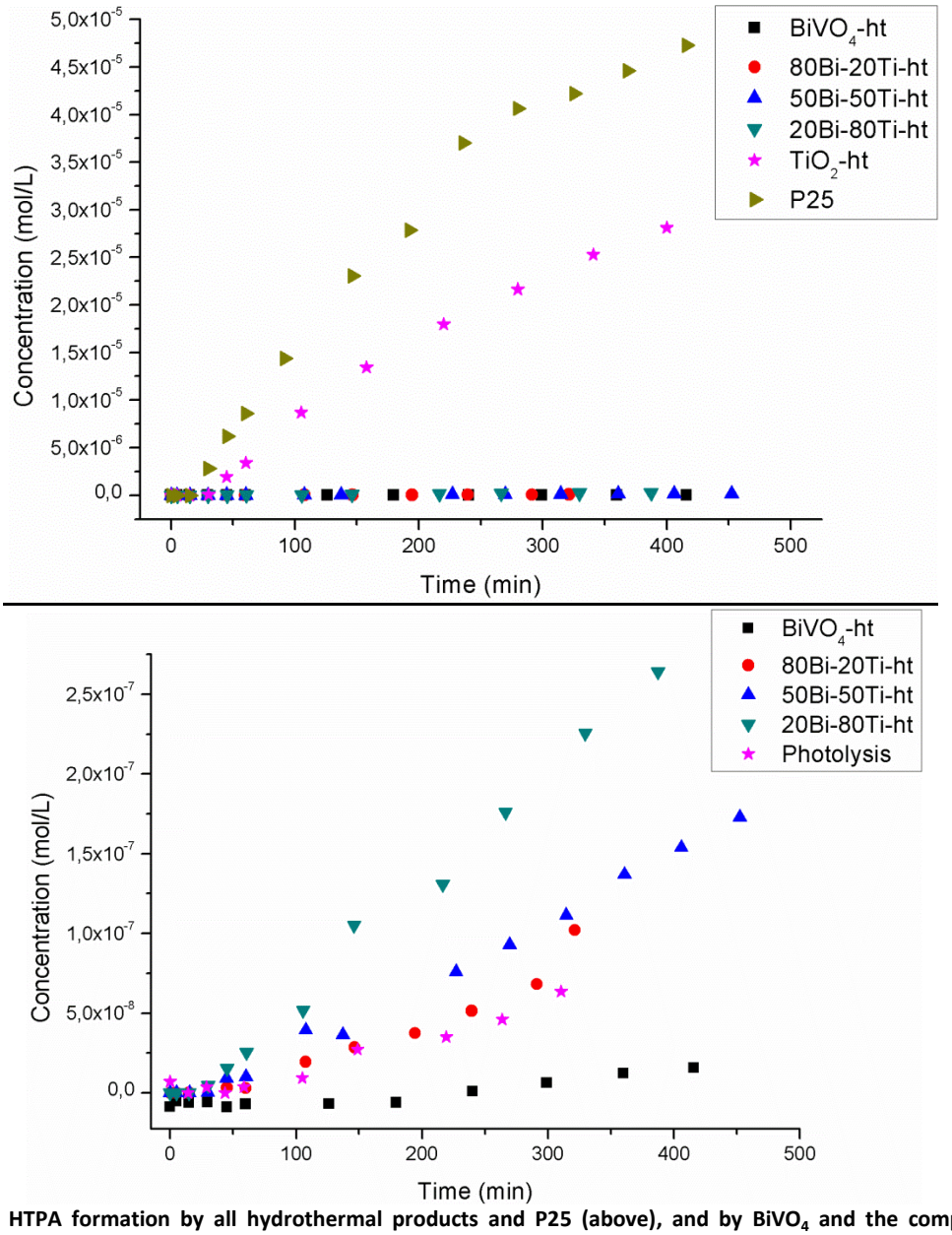

Fig. 31 HTPA formation by all hydrothermal products and P25 (above), and by $BiVO_4$ and the composite (below)

Sample	K (mol/L*min)
$BiVO_4$-ht	9,3E-11
80Bi-20Ti-ht	3.0E-10
50Bi-50Ti-ht	4.1E-10
20Bi-80Ti-ht	7.3E-10
TiO_2-ht	8.4E-8
P25	1.9E-7
Photolysis	2.3E-10

Tab. 9 Rate constant of the formation of HTPA by hydrothermal products

The formation of HTPA does not follow a linear relationship with time of irradiation, but it reaches a plateau, after that the concentration of HTPA starts to decrease. The equation that describes this trend is:[69]

$$\frac{d[HTPA]}{dt} = k_1 - k_2[HTPA]$$

In the initial part of the curve, before reaching the plateau, the proportionality can be considered linear and the degradation of HTPA can be ignored; therefore the kinetic of the formation of HTPA can be approximated to a first order reaction, and the equation becomes:

$$\frac{d\,[HTPA]}{dt} = k_1$$

The rate constants listed in the table above were calculated by using this equation.
It is evident that the formation of hydroxyl radical occurs much faster in the P25 and in the TiO_2 than in the other hydrothermal products. In the composites the rate decreases as the amount of titania decreases, until the limit case of $BiVO_4$ in which there is (practically) no hydroxyl radical formation, as reported by some other groups.[20, 32] For these type of lamps (as for the lamps used in the photocatalytic reactor), the amount of UV emission was measured using the sensor SunCal BB 300-400 BST (Atlas), that revealed an emission of UV light (in the region between 300 and 400 nm) of 0.2W/m^2.

4.2.2 Calcined products

<u>Gas phase reaction</u>
In the figure below the photocatalytic activity test are reported, and in Tab. 10 the rate constants are listed.

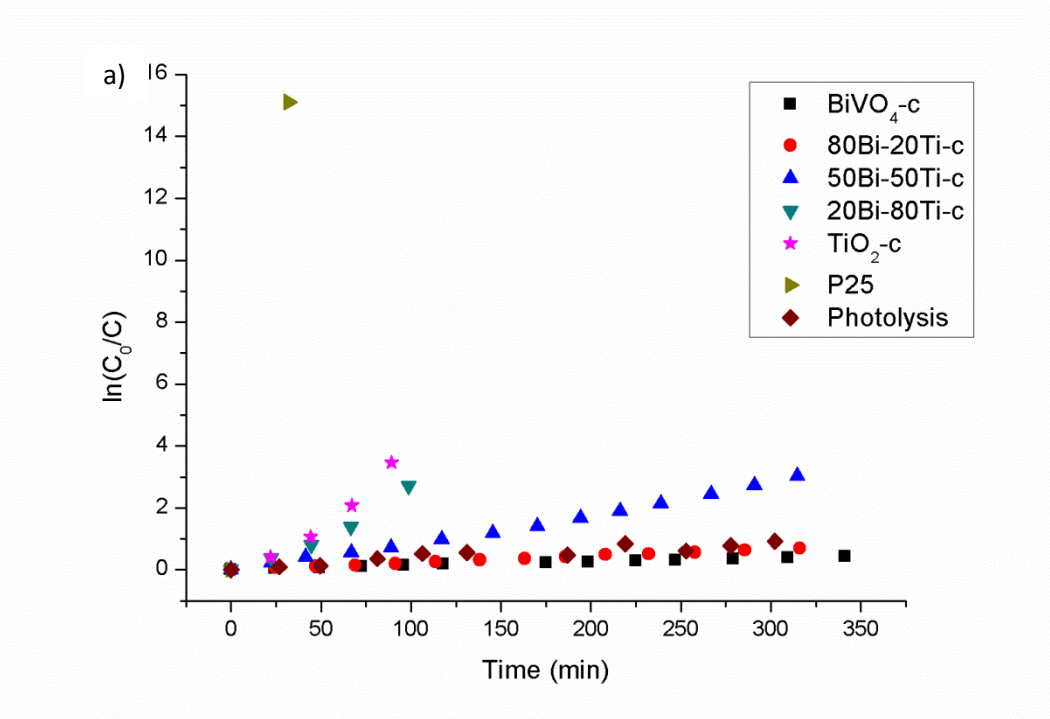

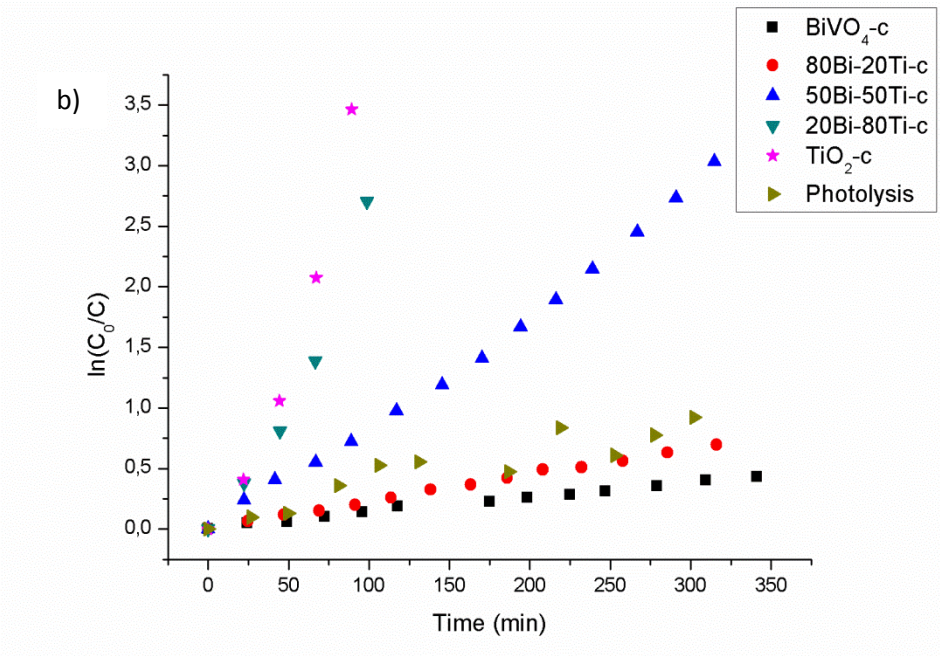

Fig. 32 a) Rate curves of all the thermal compounds toward the degradation of isopropanol; b) Rate curves of the thermal compound without P25

NAME	K (min^{-1})
$BiVO_4$-c	1.2E-3
80Bi-20Ti-c	2.2E-3
50Bi-50Ti-c	9.4E-3
20Bi-80Ti-c	2.7E-2
TiO_2-c	3.9E-2
P25	4.7E-1
Photolysis	2.7E-3

Tab. 10 Rate constant of the degradation of isopropanol by thermal products

As it can be seen from the graph below, P25 is the most active catalyst.

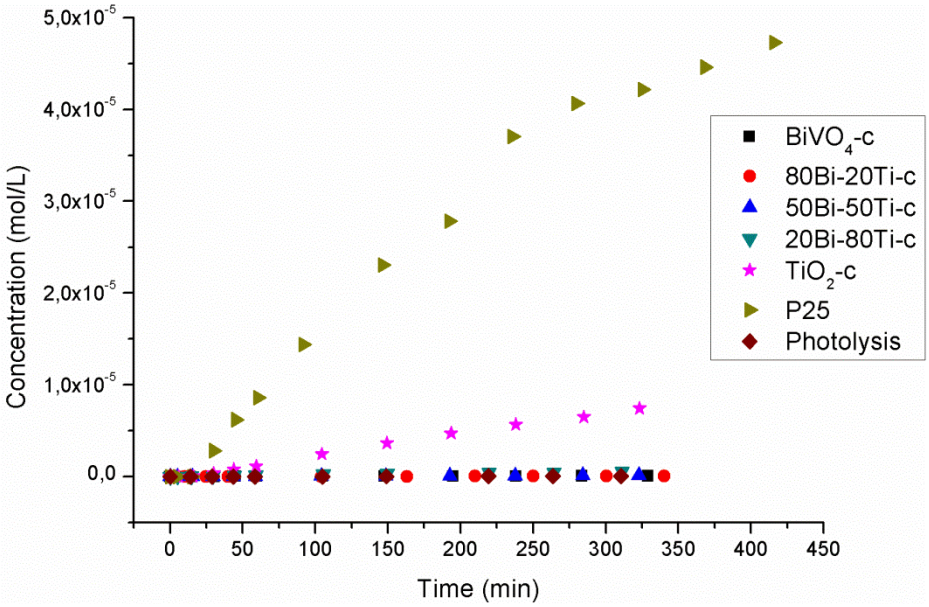

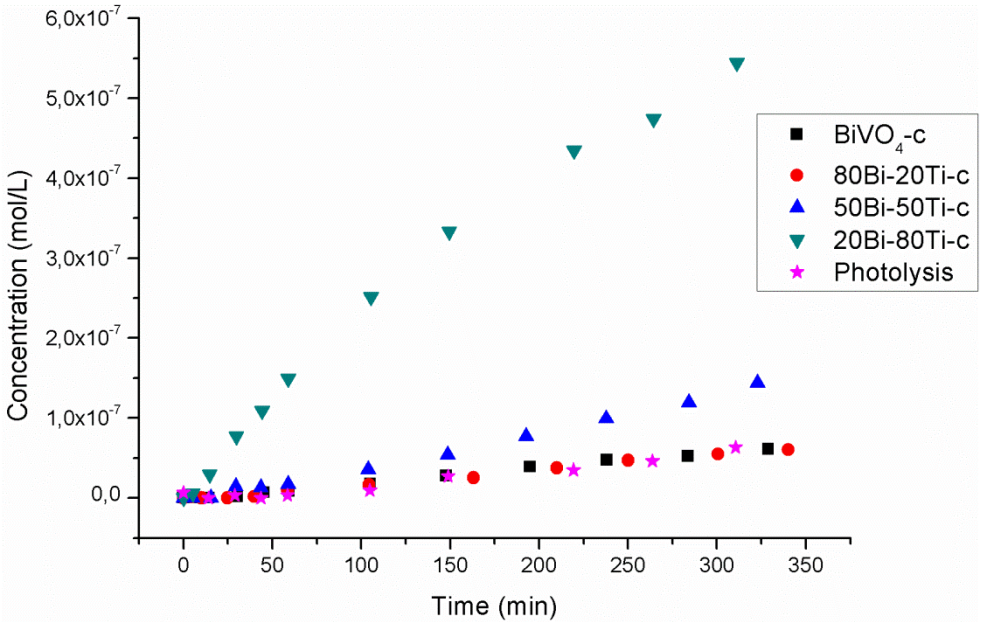

Fig. 33 HTPA formation by all thermal products and P25 (above), and by $BiVO_4$ and the composite (below)

Fig. 33 reports the formation of HTPA, while the table below lists the obtained rate constants.

Sample	K (mol/L*min)
$BiVO_4$-c	2.1E-10
80Bi-20Ti-c	1.9E-10
50Bi-50Ti-c	4.2E-10
20Bi-80Ti-c	1.8E-9
TiO_2-c	2.4E-8
P25	1.9E-7
Photolysis	2.3E-10

Tab. 11 Rate constants of the HTPA formation

4.3 Photocatalytic activity evaluation

First of all is necessary to make a clarification of the constant values reported both for the degradation of isopropanol and for the formation of HTPA, for all the catalysts, hydrothermal and calcined. In Tab. 8, 9, 10 and 11 also the photolysis constants are reported. The photolysis consists in the degradation of the pollutant through the cleavage of one or more covalent bonds resulting from absorption of light, without using any catalyst.[29] These values were evaluated by assuming that also the photolysis occurs with the same kinetic model of the photodegradation. This assumption was made for comparative purpose and considering that a good correlation coefficient with the logarithmic plot was obtained. The photolysis rate constant is higher than the constant of $BiVO_4$ and for the calcined products is also higher than the 80Bi-20Ti-c. Claiming that bismuth vanadate slows down the photolytic process is not realistic, and for this reason the difference between the photolytic rate constant and the $BiVO_4$ one must be considered as the experimental error.

In addition in Tab. 8, reporting the rate constants of the photocatalytic degradation, there is a sample called bilayer, *i.e.* the deposition of a layer of $BiVO_4$-ht over a TiO_2-ht layer.

From the graphs in Fig. 30 and 32 and from the constants reported in Tab. 8 and 10, it is evident that the P25 is the most active catalyst, followed by TiO_2, both in the hydrothermal and in the calcined products for the degradation of isopropanol. This can be a consequence of the composition of P25. In fact, as mentioned in Chapter 3.2, the presence of both anatase and rutile phase, enhance the photocatalytic activity as consequence of the building up of a p-n junction.

The graphs below represent the rate constant of each class of products against the amount in titania.

a)

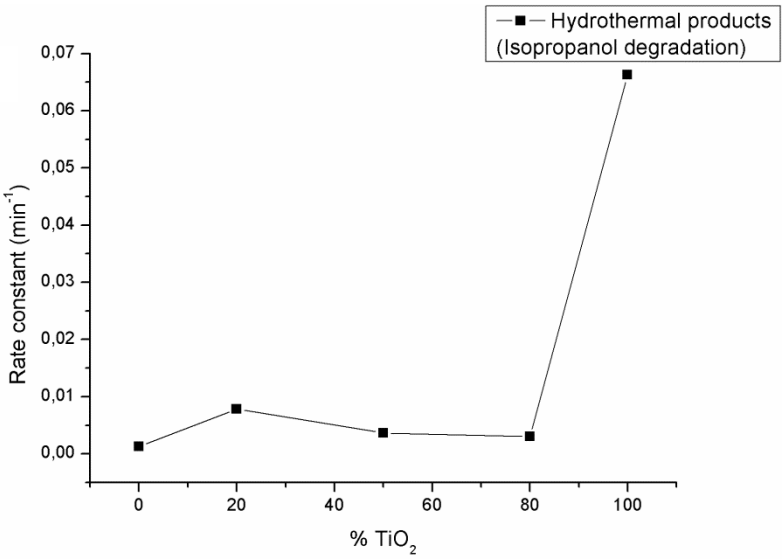

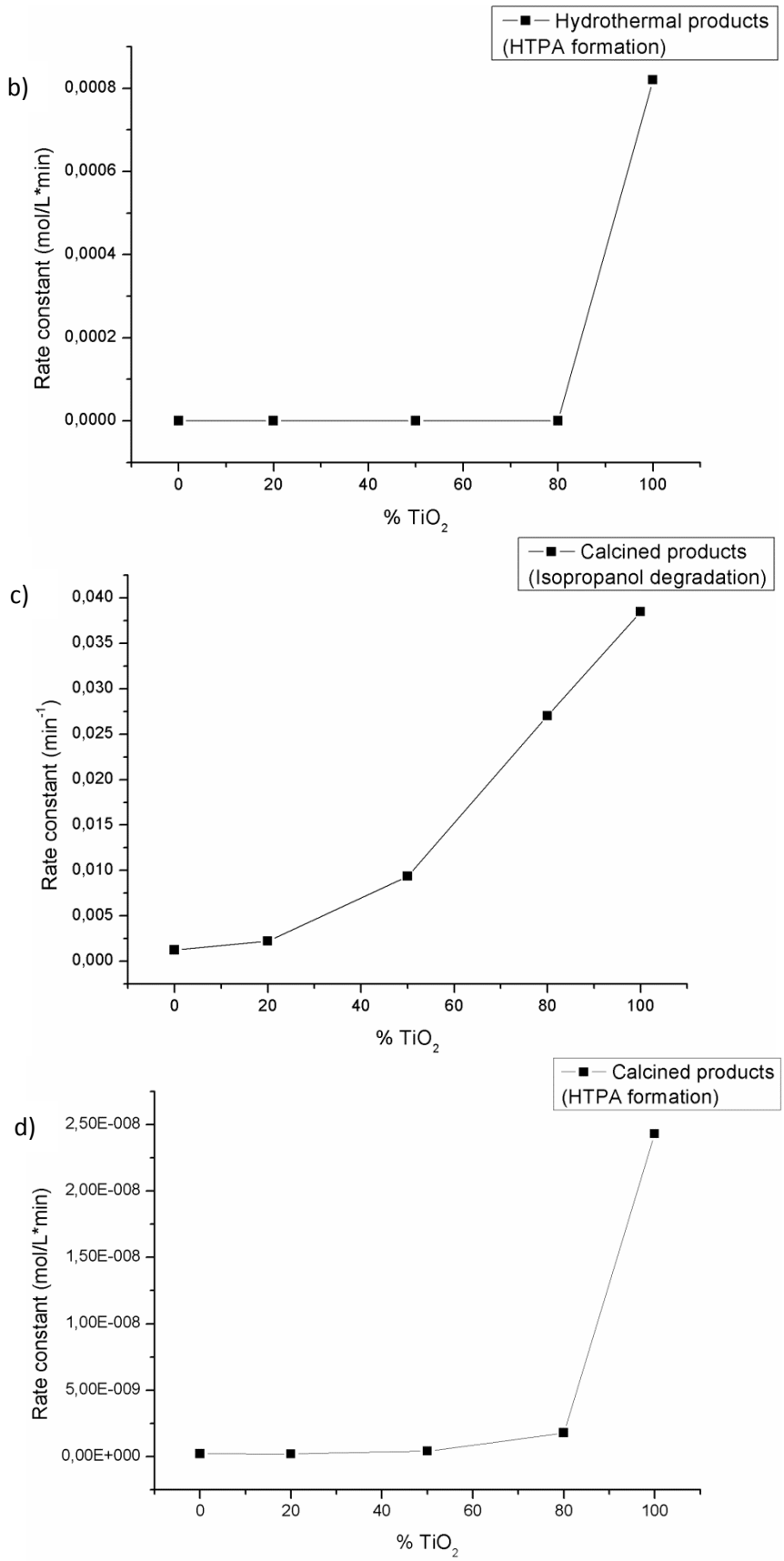

Fig. 34 Isopropanol degradation constant by hydrothermal (a) and thermal products (c) and HTPA formation constant by hydrothermal (b) and thermal (d) products, plotted against the quantity of TiO_2

The first conclusion that can be inferred from these graphs, is that $BiVO_4$ does not improve the photocatalytic activity of titania under this type of illumination. In fact,

it can be seen from Fig. 34-c that the photocatalytic kinetic constant increases as the amount of titania increases. For the hydrothermal products the trend among the composites is inverted, but it is doubtless that $BiVO_4$ and the composites have smaller constants than 100% in TiO_2.

For both classes of composites (hydrothermal and thermal) the amount of HTPA increases as the amount of titania increases, even if this can not be inferred from the graphs reported in Fig. 34, but it can be appreciated considering the values of the constants. This suggests that the production of hydroxyl radical is due to the presence of titania, not to bismuth vanadate. Consequently, if the hydroxyl radical attack were the main path of degradation of the pollutant, the activity in the degradation of isopropanol would become bigger and bigger as the amount of titania increases. This hypothesis is however not confirmed by the hydrothermal products, as explained before. This could be explained by assuming that in the hydrothermal products the main path of degradation of isopropanol does not occur towards hydroxyl radical attack, but with another mechanism. It can be also supposed that a deactivation of the catalytic surface occurs, but the presence of adsorbed organic molecules on the catalyst surface, that can inhibit the activity of the catalyst, is excluded by FT-IR spectra (performed on catalyst powders after the photocatalytic test) which revealed no signals from organic compounds.

The low activity of bismuth vanadate (obtained both from hydrothermal and form thermal synthesis) can be ascribed to the low specific surface area, as revealed from BET analysis. The low activity of the composites does not derive from different phases in the composites, since the XRD diffractograms confirm the achievement of monoclinic scheelite for bismuth vanadate and anatase for titania in all the compounds.

In the calcined products, the photocatalytic activity increases accordingly to the specific surface area, while in the hydrothermal samples the photocatalytic activity follows the opposite trend with respect to BET specific surface area. These considerations are graphically reported in Fig. 35

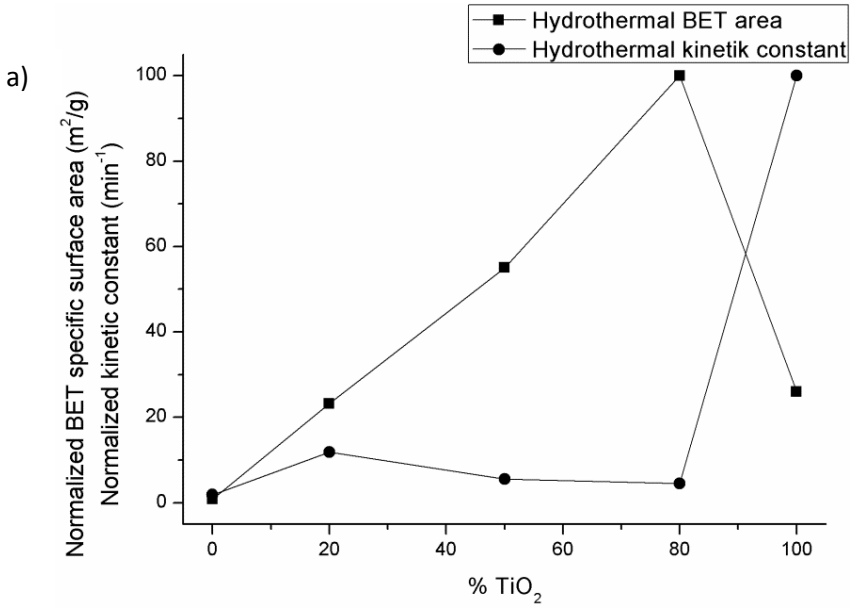

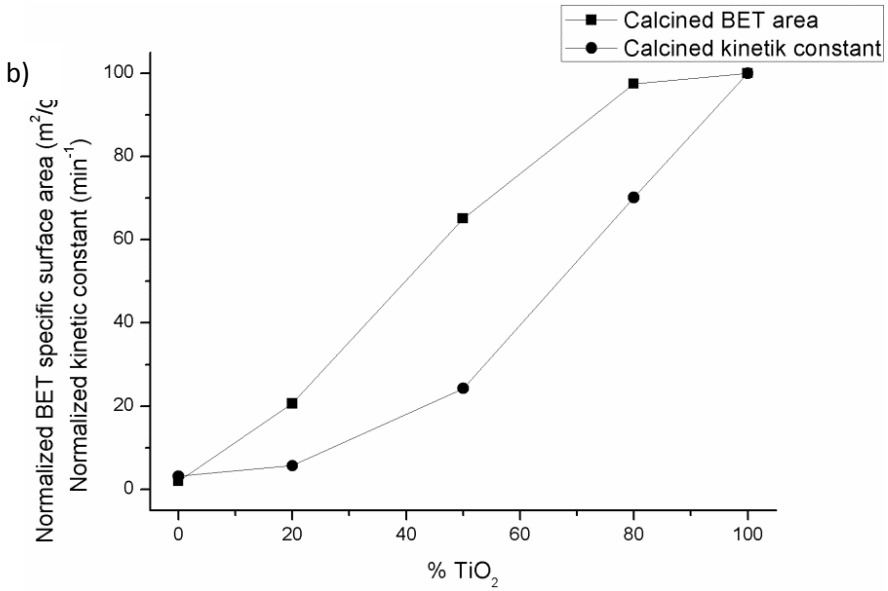

Fig. 35 BET specific surface area and photocatalytic kinetik constant reported together for a) hydrothermal products and b) thermal products

Even if it is proved that the specific surface area is directly related to the photocatalytic activity, for the hydrothermal compounds this proportionality is not respected.

The bilayer had a weight ratio of 55% in $BiVO_4$ and 45 % in TiO_2, so the activity should be similar to the kinetic constant of the 50Bi-50Ti-ht. Instead the constant of the hydrothermal bilayer is twice the constant of 50% hydrothermal composite. From the XPS analysis of the 50Bi-50Ti-ht sample it results that titania tends to enrich on the surface of the composites having the 20 and 50 percent of titania. In the bilayer the situation is reversed, since the $BiVO_4$ is deposited on the TiO_2. This could lead to an improved absorption of the light with the consequent observed enhancement of the photocatalytic activity under this type of illumination.

With the most active photocatalysts (that is P25, TiO_2-ht, TiO_2-c 20Bi-80Ti-c and the bilayer) it is also possible to see the intermediate nature of acetone. In Fig. 36 the concentration of acetone (using TiO_2-c as photocatalyst) is plotted against time.

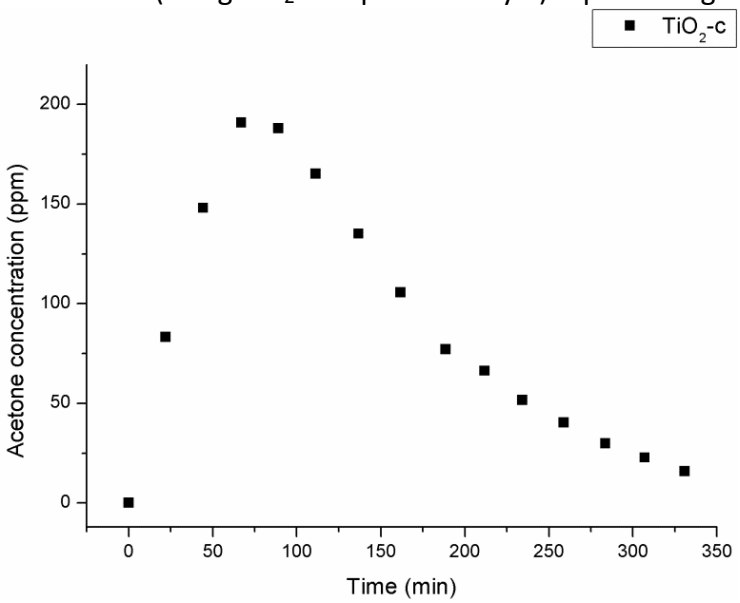

Fig. 36 Acetone concentration during the photocatalytic test.

Acetone is the first product of degradation of isopropanol and, for this reason, its concentration increases during the beginning of the reaction. After a period of accumulation, acetone starts to disappear, being degraded to other compounds, such as acetic acid (revealed by the gas chromatograph for some photocatalysts) and eventually CO_2. These steps of the isopropanol degradation are not consequential. The accumulation of acetone does not last until the total disappearance of isopropanol, as acetic acid does not start to be evident when the concentration of acetone decreases. All these phenomena occur simultaneously, and this highlights the difficulty to rationalize all the mechanisms that take place on the catalyst surface.

5. Experimental section

$Bi(NO_3)_3*5H_2O$ and NH_4VO_3 were purchased from Alfa Aesar, and used without any further purification.
$Ti[OCH(CH_3)_2]_4$ was purchased from Fluka, and used without any further purification.

5.1 Synthesis

5.1.1 Hydrothermal synthesis of $BiVO_4$ and TiO_2

$BiVO_4$ ($BiVO_4$-ht)
Two solutions were prepared: solution A containing 5 mmol of $Bi(NO_3)_3*5H_2O$ in 10 ml of 4M HNO_3, and solution B, with 5 mmol of NH_4VO_3 in 10 ml of 2M NaOH. When both salts were dissolved, solution B was poured in solution A, forming an intense orange solution. The pH of the solution was basified to 7 using 2M NaOH, and controlling the value through a pH-meter. Upon the basification, the change of color from orange to yellow is evident, as well as the formation of a yellow solid. After basification, the solution was left stirring for 30 minutes and then was put in two autoclaves, each with 28 ml of volume, and put in the oven at 180 °C for 24 hours. After this time the autoclaves were cooled at room temperature and finally opened. A yellow solid with colorless mother liquid was recovered. The solid was washed three times with bidistilled H_2O and once with EtOH, and centrifugated at 9500 rpm for 15 minutes to separate the powder from the washing liquid. Then the $BiVO_4$ was left drying in air for one night, and after in the oven at 100 °C for two hours.

TiO_2 (TiO_2-ht)
1.48 ml of titanium isopropoxide was peptized in 17.76 ml of bidistilled water with 0.127 ml of concentrated HNO_3 at 40 °C for 24 hours. After this time, the solution was basified to pH 7 using 2M NaOH and a pH-meter. The obtained white sol was left stirring for 30 minutes, and then poured in the autoclaves. These were sealed and put in the oven at 180 °C for 24 hours. After the treatment, the formation of a white solid in a colorless liquid was observed. The powder was washed three times with bidistilled water and once with EtOH, and always separated by centrifugation at 11000 rpm for 15 minutes. The so-obtained solid was left drying at air for one night and in oven at 100 °C for two hours.

5.1.2 Hydrothermal synthesis of the composites

Three composites of $BiVO_4/TiO_2$ were produced, characterized by different nominal weight ratios: 20% $BiVO_4$-80% TiO_2 (20Bi-80Ti-ht), 50% $BiVO_4$-50% TiO_2 (50Bi-50Ti-ht), 80% $BiVO_4$-20%TiO_2 (80Bi-20Ti-ht). A sol of titania was prepared by peptization of $Ti(O^iPr)_4$ in acidic water for 24 hours, as explained before. Also the $BiVO_4$ precursor was produced as mentioned in the previous chapter, preparing solution A and B and mixing them together. Then the titanium dioxide sol was poured in the vessel containing $BiVO_4$ precursor; the relative amounts were calculated in order to obtain the desired proportion in the final product.

After $BiVO_4$ and TiO_2 precursors were mixed together, the whole solution was basified to pH 7 using NaOH 2 M and a pH-meter, and was left stirring for 30 minutes. Then the autoclaves were filled with this solution, and were put in the oven at 180 °C for 24 hours. After this time the sealed vessels were opened, and a solid with colorless liquid was recovered. The color of the solid changes with the amount of titania, ranging from yellow for 80Bi-20Ti-ht to beige with the composite with 80% of titania. All the solids were washed three times with bidistilled water, and once with EtOH, centrifugated in order to separate solid and liquid, left drying in air for the night and finally dried at 100°C for two hours.
The centrifugation speed was 11000 rpm for the composites with the highest amount of titanium dioxide, while was 9500 rpm for the others. Two different speed of centrifugation were used because titania tends to form smaller crystallite than bismuth vanadate, and smaller particles required higher speed to precipitate if compared with bigger particles.

5.1.3 Thermal synthesis of $BiVO_4$ and TiO_2

$BiVO_4$ ($BiVO_4$-c)
The preparation of the precursor solution of bismuth vanadate is the same as the one for the hydrothermal synthesis: solution B of NH_4VO_3 was poured in solution A of $Bi(NO_3)_3*5H_2O$. The orange suspension was basified to pH 7 with NaOH 2M, and was left stirring for 15 hours. The basification causes the precipitation of the solid, that was washed here times with bidistilled water and once with EtOH and separated by centrifugation at 9500 rpm. The yellow solid (dried in air for one night) was put in the furnace, where it was heated up to 500 °C in 40 minutes and it was calcined at that temperature for 3 hours.

TiO_2 (TiO_2-c)
The first step consists in the peptization of titanium isopropoxide in acidic water, as mentioned previously. After 24 hours of stirring the sol was basified to pH 7 using NaOH 2M, and the suspension was left stirring for 30 minutes. The TiO_2 powder precipitated after the increasing of pH was washed three times with bidistilled H_2O and once with EtOH, and separated from the liquid by centrifugation at 11000 rpm after each washing.
Once the solid obtained was dry, it was calcined at 500 °C for 3 hours; the temperature was reached from room temperature in 40 minutes.

5.1.4 Thermal synthesis of the composites

Three composites of $BiVO_4/TiO_2$ were synthesized with different weight ratios: 20% $BiVO_4$-80% TiO_2 (20Bi-80Ti-c), 50% $BiVO_4$-50% TiO_2 (50Bi-50Ti-c) and 80% $BiVO_4$-20% TiO_2 (80Bi-20Ti-c).
In a sol of titania obtained through peptization of $Ti(O^iPr)_4$ as described before, $BiVO_4$-ht was added and mixed together. The quantities of $BiVO_4$-ht were calculated in order to obtain the desired weight ratio in the final product. The pale yellow suspension (made by TiO_2 and $BiVO_4$) was basified to pH 7 with NaOH 2M, and was left stirring for 15 hours. Then the solution was washed three times with bidistilled H_2O and once with EtOH, centrifugated to separate the two phases and left drying

at air for one night. The centrifugation speed was 11000 rpm for the composites with the highest percentage of TiO_2, while it was 9500 rpm for the other two composites, for the reasons explained above. The dry composites were calcined for three hours at 500 °C.

5.1.5 Synthesis of $BiVO_4$ from citrate precursors ($BiVO_4$-ct)

Solution A was produced by dissolving 0.01 mol of $Bi(NO_3)_3*5H_2O$ in 50 ml of bidistilled water with 10% w/w of HNO_3; after dissolution of the salt, 0.02 mol of citric acid were added. In solution B, 0.01 mol of NH_4VO_3 were dissolved in boiling NaOH 0.05 M. After dissolution of ammonium metavanadate, 0.02 mol of citric acid were added; the solution became orange, whereas after cooling a yellow-green color appeared. Solution A was then added into B, and left under stirring until the color does not change anymore. The resulting solution, in fact, became light green, then it turned to dark green until it reached a dark and intense blue. The dark blue solution was basified with ammonia solution up to pH 6.5. The system was heated at 80 °C until a dark blue foam was formed. This foam was finally calcined at 500 °C for three hours, and that temperature was reached with a slow ramp, in three hours. The solid, after calcinations, changed color, from blue to yellow.

5.2 Photocatalytic reactions

The photocatalytic activity of the obtained catalysts was tested following the degradation of isopropanol. A scheme of the used equipment is reported below.

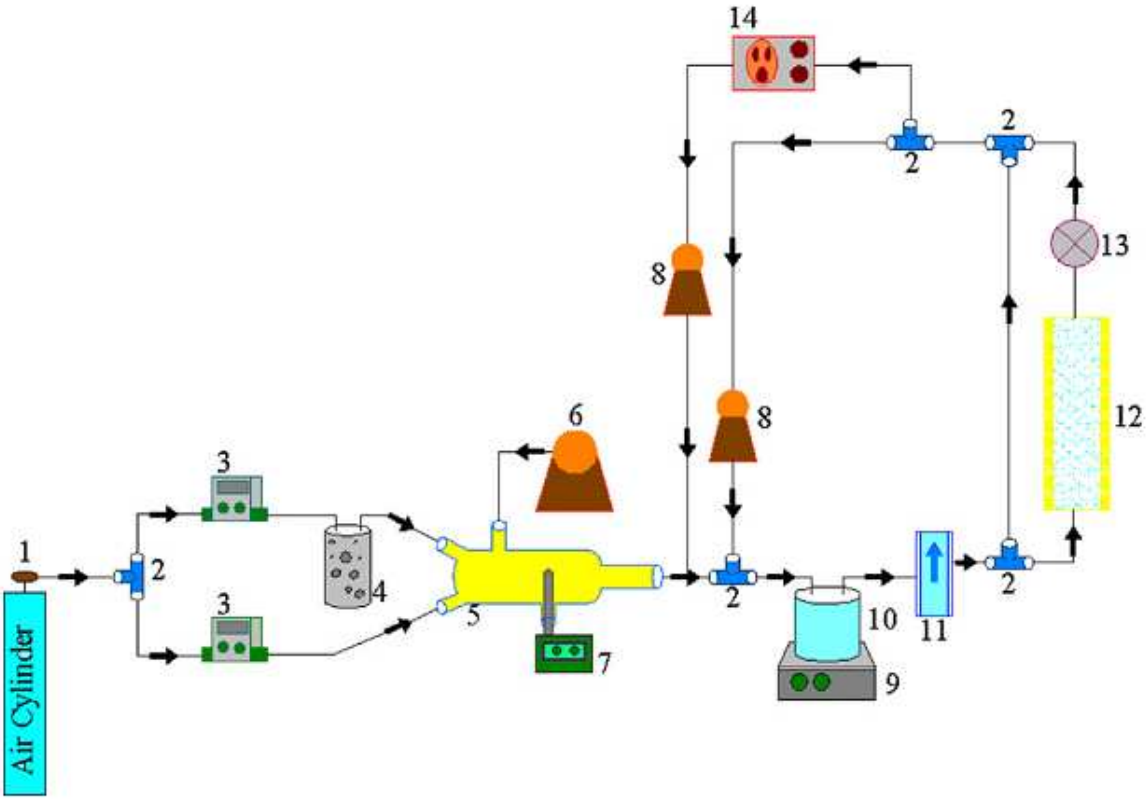

Fig. 37 Schematic diagram of the set-up for the gaseous photocatalysis: (1) gas regulator, (2) 3-way valve, (3)mass flowmeter/controller, (4) humidifier, (5) mixing chamber, (6) syringe pump, (7) termomether, (8) diaphragm pump, (9-10) reservoir vessel, (11) flow meter, (12) reactor cell with surrounding Vis lamps, (13) sampling port, (14) GC-MS[70]

Description of the system

The left part of the scheme represents the feed of the reaction; it is formed by a mixing room where synthetic air, which comes from the mass flow controllers (Aalborg AFC 26), is mixed with isopropanol, coming from the syringe pump (TSE System). The air flow is divided in two parts, one that goes directly to the mix chamber and the second one that goes through a bottle containing deionized water. The flow rates of both dry and wet air are set on 0.2 l/min, in order to obtain a total flux of 0.4 l/min with the 45-50% of relative humidity. The flow rate of the syringe pump is 0.25µl/min. The mixing chamber consists in a 30 cm long and 3 cm of outer diameter Duran glass tube.

The right part represents a reaction loop. There are two diaphragm pumps (Sensortechnics GmbH) the first one to circulate the mixed gas through the circuit, the latter to sample the gas phase to the on-line GC-MS (Varian). The compact reactor chamber has the dimensions of 35.5 cm x 35.5 cm x 20.5 cm, with the inner part completely covered with polished aluminum, in order to guarantee the reflection of the light coming from six daylight lamps (Osram L 8W/954) of 8 W each one. In the middle of the chamber there is the glass reaction cell, formed by a tube with the dimensions of 36 cm of length and 5 cm of outer diameter. In the reaction cell there was a glass rod coated with the desired catalyst. The coating procedure will be discussed in the following paragraph.

Photocatalytic experiments

In a typical procedure, the accumulation of the feed lasted around 16 hours (over night), and during this period the gas flowed from the mixing chamber to the reservoir vessels through the flow meter. When the desired amount of isopropanol in the reservoir vessel was reached, the air flux and the syringe pump were switched off, and the pumps on the right part of the scheme were switched on. The irradiation started after achieving the adsorption-desorption equilibrium between the gas phase and the catalyst layer. The reaction was followed by constant time intervals sampling and analyzing with a gas chromatographer (Varian 3900) coupled with a mass spectrometer (Varian Saturn 2100 T) operating in an electron impact (EI) mode and with a ion trap analyzer. The column was plot fused silica 25m x 0.32mm id coating CP-porabond U, and the carrier gas was helium. The sampling was performed every 15 minutes for the first two hours, then every hour for a total reaction time of at least five hours.

Calibration of the system

The GC-MS coupled with the gas-phase reactor was calibrated using both ispropanol and acetone. The humidifier (n°. 4 in Fig. 37) was filled with isopropanol or acetone, with analytical grade purity, and was put into an insulated vessel containing ice and sodium chloride. A thermometer revealed in continuum the temperature of the system. In the mixing chamber (n°. 5) the saturated vapor of isopropanol or acetone was mixed with synthetic air, in order to dilute ten times the concentration of the analyte. For each solution three injections were performed at different temperatures. The partial pressure of the gaseous isopropanol or acetone was calculated through the Antoine equation:[71]

$$\log P = A - \frac{B}{T + C}$$

Where P is the partial pressure expressed in mmHg, T is the temperature in °C and A, B, C are three parameters, different for each substance. The table below lists the parameters for the two substances.[72]

	Isopropanol	**Acetone**
A	8.1182	7.2316
B	1580.92	1277.03
C	219.62	237.23

Tab. 12 Parameters for the Antoine equation for isopropanol and acetone

Once that the partial pressure is obtained, it is possible to calculate the molar fraction (and the volumetric concentration) through the partial vapor pressure definition:

$$P_i = PX_i$$

The calibration was finally carried out by plotting the area of the chromatogram versus the concentration of analyte, and forcing the intercept to zero. The so-obtained calibration curves are reported below:

Isopropanol Area = 286.26*Concentration
Acetone Area = 259.95*Concentration

Coating method

This method was used to deposit the catalysts on glass bars for the photocatalytic experiments. The catalyst was deposited on the glass rod through a brush technique. The photocatalysts were wetted with the minimum possible quantity of absolute ethanol, in order to form a slurry. This was then applied on the glass using a brush, rapidly dried with an air drier and put in the oven at 150 °C for one hour. While with titania it was possible to deposit another layer on the dried one, with $BiVO_4$ and the composites this second step was not possible (because the second application removed the first one), so the correct quantity of catalyst should be deposited in just one application. Also the deposition of a bilayer was performed. First TiO_2-ht was deposited on the bar and over it a layer of $BiVO_4$-ht was laid, with a weight ratio of TiO_2 of 44%.
In Tab. 13 the type of catalyst and the mass of catalyst are reported

Sample	Mass of catalyst (g/cm^2)	Time of irradiation (hours)
$BiVO_4$-ht	1.16	5.40
80Bi-20Ti-ht	0.98	7.15
50Bi-50Ti-ht	1.43	5.30
20Bi-80Ti-ht	0.98	5.00
TiO_2-ht	0.92	5.10
$BiVO_4$-c	1.42	5.30
80Bi-20Ti-c	0.93	5.15
50Bi-50Ti-c	0.97	5.15
20Bi-80Ti-c	1.15	5.15
TiO_2-c	1.00	5.30
P25	0.93	5.10
Bilayer	1.11	5.30
Photolysis	-	5.00

Tab. 13 Name, mass, and time of irradiation during the photocatalytic experiments

5.3 HTPA fluorescence protocol

The formation of the highly fluorescent hydroxyterephtalic acid (HTPA) from terephtalic acid (TPA) was followed by fluorescence measurements, in order to monitor hydroxyl radical formation.[69, 73] This is possible thanks to the reaction between hydroxyl radical and terephtalic acid, reported below:

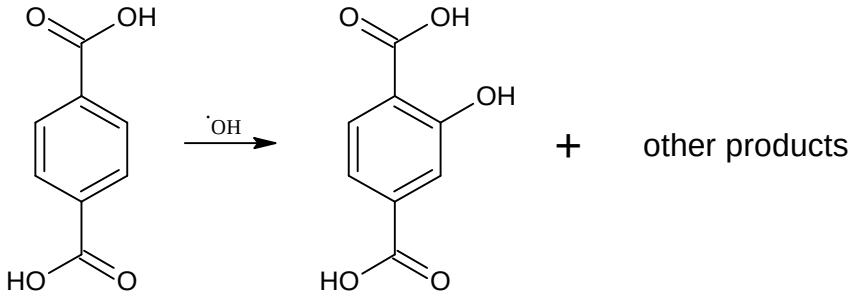

Fig. 38 Reaction of formation of HTPA

This reaction leads to the formation of HTPA and other products. Nevertheless only HTPA is detected due to its fluorescence.

Description of the system

The system for HTPA measurements was formed by a box of 70x30x40 cm^3 with the lower part that can be opened (to put samples inside and outside), and containing in the upper part a Sylvania lamp (standard F18W/154 daylight, 18 W) and two Osram lamps (L 15W/84C cool white, 15 W). To check the quantities of HTPA in the sampled samples, fluorescence measurements were performed, with Tecan infinite F200 microplates reader with fluorescence detection.

Practical procedure

All the chemicals were used as received without any further purification. 40 ml of $5*10^{-4}$ M TPA in $2*10^{-3}$ M NaOH aqueous solution were put in a beaker, together with 20 mg of the desired catalyst. The solution was stirred in the dark for 15 minutes, then the irradiation started and samples were taken at established times:

0 (the moment of uncovering), 5, 15, 30, 45, 60 minutes and then every hour or every 45 minutes for a total reaction time of at least 5 hours.
The sampling was performed by using a 1 ml syringe, and the solution was put in a obscured Eppendorf vial. Then the vials were centrifugated with a Mini Spin Eppendorf centrifugue, at the speed of 9500 rpm for 10 minutes, in order to separate the liquid and the catalyst. From each Eppendorf, 0.159 ml were taken with a micropipette, put in a plate and read by the microplate reader. The data of the experiments are collected in the table below.

Name of catalyst	**Mass of catalyst (mg)**	**UV irradiance (W/m^2)**	**Time of irradiation (hours)**
$BiVO_4$-ht	22.6	0.2	7.0
80Bi-20Ti-ht	21.0	0.2	5.2
50Bi-50Ti-ht	20.7	0.2	7.5
20Bi-80Ti-ht	20.3	0.2	6.5
TiO_2-ht	20.8	0.2	6.5
$BiVO_4$-c	20.9	0.2	5.3
80Bi-20Ti-c	21.3	0.2	5.4
50Bi-50Ti-c	21.3	0.2	5.2
20Bi-80Ti-c	21.2	0.2	5.1
TiO_2-c	22.1	0.2	5.2
P25	20.6	0.2	7.0
Photolysis	-	0.2	5.1

Tab. 14 Name of catalyst, its mass, irradiance and time of irradiation during the TPA-HTPA experiments.

6. Characterization techniques

6.1 X-Ray Diffraction (XRD)

X-Ray diffraction is a technique used to investigate crystalline solids. It can be used to analyze both single crystals and polycrystalline powders based on the diffraction phenomenon, using the electronic clouds as diffraction centers.
To understand how this technique works it is useful to have a simple representation to obtain some basic concepts. First of all is necessary to explain the concept of crystallographic planes and reciprocal lattice, since they are very useful for the description of the signal collected by the diffractometer.
A set of crystallographic planes *hkl* are a set of equidistant planes, one of which passes through the origin and the next nearest one makes intercepts a/*h*, b/*k*, c/*l* on the three crystallographic axes **a**, **b** and **c**. The integers *h*, *k* and *l* are called the Miller indices.
The reciprocal lattice is defined as the lattice formed by repetition of reciprocal vectors **a***, **b*** and **c***, defined as:[74]

$$\mathbf{a}^* = \frac{\mathbf{b} \times \mathbf{c}}{\mathbf{a} \cdot \mathbf{b} \times \mathbf{c}}$$

$$\mathbf{b}^* = \frac{\mathbf{c} \times \mathbf{a}}{\mathbf{a} \cdot \mathbf{b} \times \mathbf{c}}$$

$$\mathbf{c}^* = \frac{\mathbf{a} \times \mathbf{b}}{\mathbf{a} \cdot \mathbf{b} \times \mathbf{c}}$$

Where **a**, **b**, **c**, are the crystallographic axes.
Let us imagine a series of atoms that lie on a set of crystallographic planes, and a plane wave (represented by the vector $\mathbf{s_0}$) hitting one of those atoms, as shown in figure.

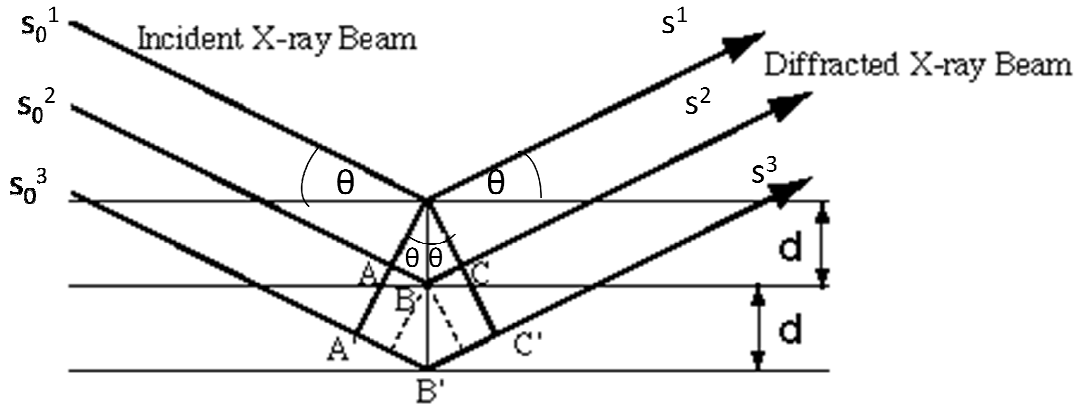

Fig. 39 Representation of the incident X-ray beam on a schematic set of planes

In order to have a constructive interference, the additional path made by $\mathbf{s_0}^2$ and $\mathbf{s_0}^3$ (compared to the one made by $\mathbf{s_0}^1$) must be an integer multiple of the wavelength. If this condition is not respected, a destructive interference always occurs. The additional path is represented by AB+BC or by A'B'+B'C'. That is

$$AB + BC = 2d\text{sen}\theta$$
$$A'B' + B'C' = 4d\text{sen}\theta$$

This leads to the known form of the Bragg law:

$$2d\text{sen}\theta = n\lambda$$

This means that atoms lying on the same family of crystallographic planes (*i.e.* having the same interplanar distance), if hit by the radiation having the same wavelength, have the same diffraction angle. Because of the inherent regularity and periodicity of crystal structure, XRD analysis performs best with highly crystalline solids. In fact, with a single crystal, the highest value of regularity can be found,: since all the crystal cells are oriented in the same way, all the waves diffracted by the same family of planes will converge in the same point. These points are directly related to the position of the atoms in the reciprocal lattice.

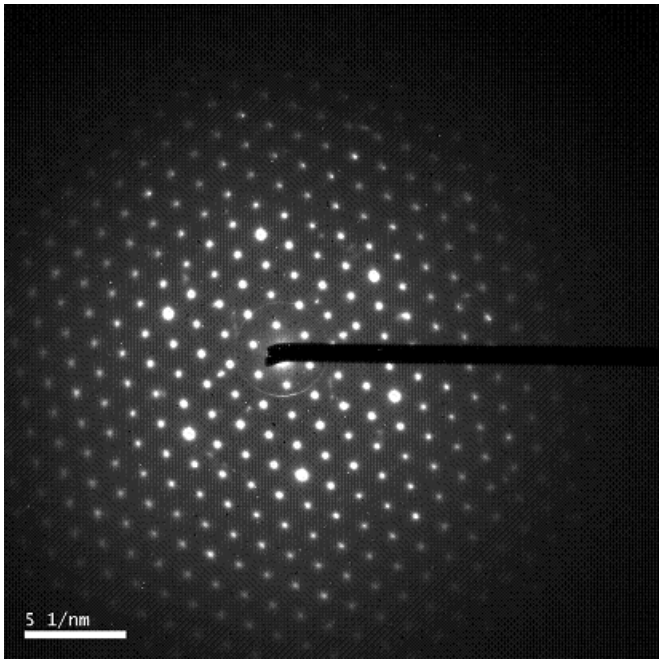

Fig. 40 Diffraction pattern of a single crystal diodati

The diffractogram collected from a polycrystalline powder sample is quite different. In a crystalline powder there are several crystalline grains oriented in all directions; thus the beams diffracted by the same family of crystallographic planes are not focused in a single point, but they will generate a cone of diffraction. Each family of planes with a different interplanar distance d_{hkl} generates a different cone.

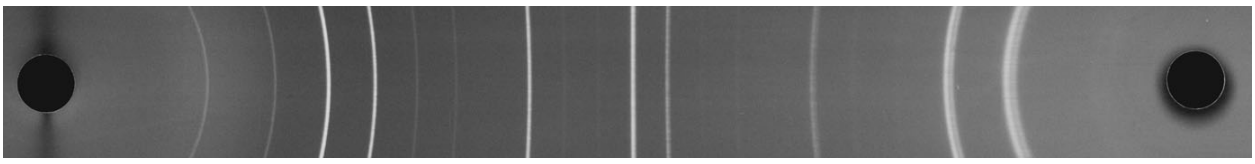

Fig. 41 Diffraction pattern of a powder diodati

The diffractograms is obtained through integration of the intensity of the cone.

From a diffractogram it is possible to calculate both the cell parameters and the average crystal size.
The calculation of the cell parameters can be performed by an iterative method, which compares both the experimental data and the theoretical structure of the crystal, seeking the best fitting between these two patterns through the variation of some parameters. This procedure was performed by using the program X'Pert HighScore version 2.1b (2.1.2).
The calculation of the average dimension of the crystals can be done by using the Scherrer equation:

$$L = \frac{K\lambda}{B(2\theta)\cos\theta}$$

Where B(2θ) is the broadening of the peak that can be approximated to the full width at half maximum, expressed in radians, λ is the wavelength of the incident beam expressed in Å, and cosθ is the cosine of the angle where the considered peak is positioned. K is a constant that considers the shape of the crystal, and the crystallite mean dimension (L) is given in Å. The so obtained value is considered as an average crystallite dimension, even if the approximation is better if the crystal size are small (tens of nanometer), because with larger crystallites the reflection shapes are more heavily influenced by other factors.
In the analyses based on electromagnetic radiation the maximum resolution that can be obtained is equal to λ/2. In addition, to have scattering, the incident wavelength has to be similar to the scattering center dimensions. Thus to study the atomic positions and to have a scattering phenomenon a radiation with wavelength in the range of the Ångstrom is necessary. The most common source of radiation is CuK_α, that has λ=1.5406Å.

6.2 X-Ray Photoelectron Spectroscopy (XPS)

X-ray photoelectron spectroscopy is a surface sensitive technique that allows to analyze the surface of solids, determining its atomic composition, the oxidation state and the chemical environment of the elements that are present in it. It is based on the photoelectric effect, and it measures the kinetic energy of an electron emitted from the surface after irradiation with X-rays (which promote a ionization from the core levels). In order to have the most reliable measurement of the kinetic energy of these electrons, the analysis must be conducted under ultra high vacuum, to avoid that the electrons hit some other particles losing its energy. Ultra high vacuum is also used to minimize the surface contamination.

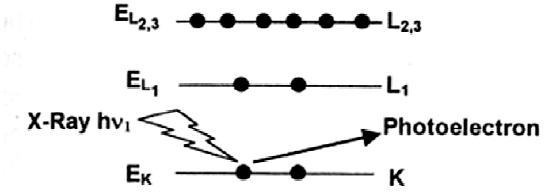

Fig. 42 Schematic representation of the photoelectron emission

Actually, the emission of primary electrons is not the only effect that can occur; in fact also phenomena of fluorescence, scattering and Auger emission can take place.[75] The last phenomenon starts with the X-ray photoelectron generation, consequence of the atom ionization. The second step is the non radiative relaxation of a more external electron to occupy the vacancy left during the first step; the release of energy during the second step permits the emission of a secondary electron, called Auger electron.[76]

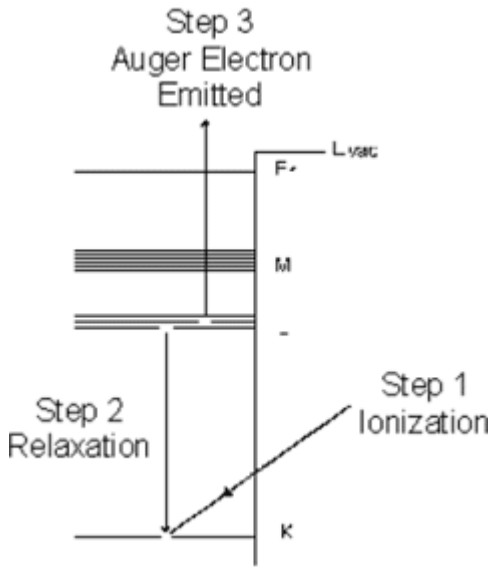

Fig. 43 Different phenomena that can occur

The process of photoemission can be summarized by the following reaction:

$$A + h\upsilon \rightarrow A^{+} + e^{-}$$

Where A is a generic atom, h the Plank constant and ν the frequency of the incident radiation.
The energy conservation principle states that:

$$E(A) + h\upsilon = E(A^{+}) + KE(e^{-})$$

By rearranging the equation taking into account the kinetic energy of the electron, the following formula is obtained:

$$KE(e^{-}) = h\nu + [E(A) - E(A^{+})] = h\nu + BE$$

This equation must be corrected with a work function of the spectrometer, so that the equation becomes:[75, 76]

$$KE = h\upsilon + BE + \phi_s$$

The binding energy is influenced both from the nature of the element, from the chemical environment and from its oxidation state. Measuring the kinetic energy, knowing the energy of the incident ray and knowing the work function of the spectrometer, it is possible to calculate the binding energy and in this way to recognize the element and its oxidation state.[77]

Usually the most common used X radiation sources are Al K_α, with 1.4866 keV of energy, and Mg K_α, having an energy equal to 1.2566 keV.[77]

6.3 Brunauer-Emmett-Teller technique (BET)

The BET analysis is a technique that yields information concerning the specific surface area of a solid material through measurements of gas adsorption. The acronym derives from the first letters of its inventors: Stephen Brunauer, Paul Emmett, Edward Teller.[78]
The quantity of adsorbed gas at constant temperature is plotted against pressure, obtaining an isotherm; all the information is then extrapolated from this curve.
The first step is to degas the sample. To do it, different routes can be used: increasing of temperature under vacuum, evaporation of the solid under vacuum and its condensation on a solid surface, breaking the crystal under vacuum in order to create new clean surfaces.[79] After the preparation of the sample, it is put in a chamber and cooled with liquid nitrogen in order to enhance the adsorption, which is an exothermic process. This passage is followed by the release of a known quantity of gaseous nitrogen in the chamber and by the registration of an adsorption isotherm. Five types of isotherm can be obtained.

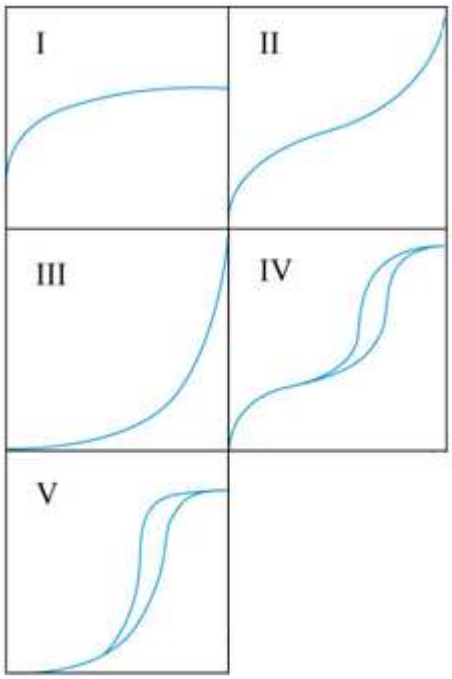

Fig. 44 Five type of isotherm. Each graph has the adsorbed volume as y axis and pressure as x axis

The I type isotherms are characteristic of the monolayer adsorption, and are well described by the Langmuir theory.[79, 80] This theory is based on some assumptions:

- The solid has a uniform surface
- There is not interaction between the adsorbed molecules
- The adsorbed molecules are localized in specific positions
- The adsorption occurs with the formation of a monolayer

The equation obtained by Langmuir is:[81, 82]

$$\theta = \frac{k_a P}{k_d + k_a P} = \frac{KP}{1 + KP}$$

Where k_a is the rate constant of the adsorption, k_d is the rate constant of the desorption P is the pressure, K is the adsorption equilibrium constant and θ is the fraction of the occupied position in the surface. The last value can be expressed also as v/v_{mon}, where v is the volume of adsorbed gas, while v_{mon} is the volume adsorbed in the monolayer, that is when the adsorbate covers all the surface of the solid.
When the pressure is low the denominator can be considered equal to 1, and the volume of adsorbed gas results linearly dependent on the pressure.
The I type isotherms are typical (but not limited) of the chemioadsorption reaction.[79]
The Langmuir theory was extended to the multilayer adsorption by Brunauer, Emmett and Teller through modification of the hypothesis, and the result is:[78-80]

$$\frac{P}{v(P^* - P)} = \frac{1}{v_{mon} c} + \frac{c - 1}{v_{mon} c} \frac{P}{P^*}$$

This equation fits well the II type isotherms, and it works also with isotherms III, IV, and V.
From this equation it is possible to estimate v_{mon}, and consequently determine the specific surface area with the following formula:

$$S = \frac{v_{mon} A_n A_m}{M_v}$$

Where A_n is the Avogadro number, A_m is the adsorption cross section of the adsorbing species and M_v is the molar volume of the gas.

6.4 UV-Vis Diffuse Reflectance Spectroscopy (DRS)

Usually optical spectroscopy delivers information on the optical measurements through the evaluation of the absorbance, by measurements of light transmission. If it is necessary to analyze a solid sample, this must be solubilized in an appropriate medium. However, this procedure can be sometimes difficult, since some solids can present low solubility, or because the optical properties of the solubilized material can be different from the solid phase. For this reason a common technique used to bypass these problems is the measurements of the reflected light, that is recording of a reflectance spectrum. The reflection can be specular or diffuse. The former case is found for smooth surfaces, in which the average dimension of the roughness is much smaller than the incident light wavelength. In this case the reflection angle is equal to the incident one. The diffuse reflection occurs in polycrystalline solids; the surface of each grain cause specular reflection, but, being the grains oriented in all the directions, also the radiation is reflected in all the directions.[83]
In this situation the parameter measured by the spectrophotometer is not transmittance anymore, but is replaced by the reflectance, defined as:[83]

$$R = \frac{I_r}{I_i}$$

Where I_R is the intensity of the reflected light, while I_i is the intensity of the incident light. The intensity of the reflected light is lower than the incident one, since absorption phenomena occur. The equation that correlates reflectance with the absorption of the solid is the Kubelka-Munk function, defined as:[83, 84]

$$F(R_\infty) = \frac{(1 - R_\infty)^2}{2R_\infty} = \frac{K}{S}$$

Where K is the molar absorption coefficient, S the scattering coefficient and R_∞ is the reflectance for a solid with infinite thickness. This value is not experimental evaluable, but it is used a relative quantity respect a white standard.[84]

$$R'_\infty = \frac{R_{sample}}{R_{standard}}$$

The molar absorption coefficient is related to the molar concentration of the analyte *c* and to the molar absorbitivity ε through the equation:[83]

$$K = 2.303 \ \varepsilon \ c$$

In this way is possible to obtain information on the absorbance of the analyte.

7. Conclusions and future perspectives

In this work $BiVO_4$, TiO_2 ad their composites with different weight ratios were synthesized by using two different synthesis routes: i) coprecipitation followed by hydrothermal treatment and ii) coprecipitation followed by thermal treatment.
The so-obtained samples were thoroughly characterized using different analytical techniques (XRD, XPS, UV-Vis spectroscopy and BET analysis) and tested for their photocatalytic activity, to obtain a comprehensive chemico-physical, structural and functional characterization.
Both the synthetic routes were proved to be effective to yield the desired phases, although the coprecipitation followed by thermal treatment produce $BiVO_4$ and TiO_2 characterized by the presence of undesired crystalline phases. The relative high temperature (500 °C) used in this route leads to the formation of rutile in the TiO_2-c samples, whereas in the XRD pattern of $BiVO_4$-c some unidentified phases were detected. In addition, the thermal treatment leads to the formation of bigger crystallites due to coalescence phenomena.
The coprecipitation followed by hydrothermal treatment provides, instead, pure phases without undesired crystalline phases, and an average size of the crystallites in general smaller than in the case of the calcined samples.
Also BET analysis shows a higher specific surface area for the hydrothermal products than for the calcined ones.
A further synthetic procedure was tested for the preparation of the pure $BiVO_4$, that is a coprecipitation followed by thermal treatment using citrate precursors. This synthesis route is however not suitable for the production of pure monoclinic bismuth vanadate, since the final product presents many spurious and unidentified phases.

The photocatalytic activity of the prepared samples was evaluated using GC-MS, and compared with the benchmark Evonik Aeroxide P25. In order to deepen the mechanistic aspects, the production of hydroxyl radical was evaluated by using fluorescence spectroscopy.
UV-Vis spectra confirm the absorption in the visible range of the mixed composites, of the $BiVO_4$-c and $BiVO_4$-ht. Nevertheless, $BiVO_4$ (both calcined and hydrothermal) does not behave like a titania sensitizer. In fact its photocatalytic activity is very low, and also the composites show lower photocatalytic activity than pure titania under indoor illumination.
This can be only partially ascribed to the low specific surface area, since the hydrothermal compounds have larger surface area than TiO_2-ht but show, however, lower photocatalytic activity. XPS analyses revealed the presence of sodium (about 10% atomic) on the surface of the compounds obtained with both the procedures. This hinting at a not completely effective purification protocol. The presence of undesired elements on the surface probably can act like recombination centers, thus determining the observed low photocatalytic activity.
The photocatalytic activity of a bilayer, prepare by depositing 55% w/w of $BiVO_4$-ht over TiO_2 layer was tested. Its photocatalytic activity is higher than the activity of the other composites, and it is very similar to the one of TiO_2-ht.

The measurements of hydroxyl radical production revealed that $BiVO_4$ does not produce the radical, and this result is in accordance with the one found by some other authors.[20]

In conclusion, although pure crystalline phases of the target compounds were obtained, the prepared composites do not show any relevant photocatalytic activity, and this lower activity can be either ascribed to the microstructure of the obtained composites or either to the presence of recombination center.

There are different improvement that can be adopted in order to improve the activity of $BiVO_4$ and, consequently, of the composites.
The firs step is an improvement of the purification protocol, in order to remove in a more efficient way the residues of precursors that can act like recombination centers for the photogenerated charges.
Another route which could be adopted would be the use of templates during the synthesis, in order to increase the porosity of the composites and, in this way, their specific surface area.
Regarding the experimental conditions, the use of lamps in the photocatalytic reactor that emit only in the visible range could allow a better evaluation of the sensitizer behavior of $BiVO_4$. In addition, an evaluation of the pore size and distribution of the samples could contribute to clarify the unexpected observed correlations between specific surface area and experimental synthesis parameters as well as between specific surface area and photocatalytic activity.
Considering the enhanced photocatalytic activity of the bilayer, another experiment could be to prepare other bilayers with a more precise coating technique and with different $BiVO_4$ and TiO_2 weight ratios, in order to rationalize the reasons for its improved functional performances.

References

1. J. M. Coronado, F. Fresno, M. D. Hernández-Alonso and P. R., *Design of Advanced Photocatalytic Materials for Energy and Environmental Applications*, Springer, 2013.
2. A. Eibner, *Chem.-Ztg*, 1911, **35**, 753-755.
3. E. C. C. Baly, I. M. Heilbron and W. F. Barker, *J. Chem. Soc.*, 1921, **119**, 1025-1035.
4. K. Hashimoto, H. Irie and A. Fujishima, *Jpn. J. Appl. Phys.*, 2005, **44**, 8269-8285.
5. C. F. Doodeve and J. A. Kitchener, *Trans. Faraday Soc.*, 1938, **34**, 902.
6. V. N. Filimonov, *Dokl. Akad. Nauk SSSr*, 1964, **154**, 922-925.
7. S. Kato and F. Maschio, *Kogyo Kagaku Zasshi*, 1964, **67**, 1136-1140.
8. A. Fujishima and K. Honda, *Nature*, 1972, **238**, 37-38.
9. S. N. Frank and A. J. Bard, *J. Am. Chem. Soc.*, 1977, **99**, 303-304.
10. O. Carp, C. L. Huisman and A. Reller, *Prog. Solid State Chem.*, 2004, **32**, 33-177.
11. S. Wang, H. M. Ang and M. O. Tade, *Environ. Int.*, 2007, **33**, 694-705.
12. J. Mo, Y. Zhang, Q. Xu, J. J. Lamson and R. Zhao, *Atmos. Environ.*, 2009, **43**, 2229-2246.
13. J. I. Pfeffer and S. Nir, *Modern Physics. An Introductory Text*, Imperial College Press, 2000.
14. N. Serpone, D. Lawless and R. Khairutdinov, *J. Phys. Chem.* , 1995, **99**, 16646-16654.
15. P. A. Tipler and R. A. Llewellyn, *Modern Physics*, W. H. Freeman and Company, 2002.
16. A. Fujishima, T. N. Rao and D. A. Tryk, *J. Photoch. Photobio. C*, 2000, **1**, 1-21.
17. ObservatoryNANO, in *'Applications of photocatalysis'*, Briefing No.10, February 2011, http://www.observatorynano.eu/project/filesystem/files/ObservatoryNANO%20Briefing%20No.10%20Applications%20for%20Photocatalysts.pdf.
18. J.-M. Herrmann, *Appl. Catal. B*, 2010, **99**, 461-468.
19. J. M. Herrmann, *Catal. Today*, 1999, **53**, 115-129.
20. M. D. Hernández-Alonso, F. Fresno, S. Suárez and J. M. Coronado, *Energy Environ. Sci.*, 2009, **2**, 1231.
21. M. R. Hoffmann, S. T. Martin, W. Choi and D. W. Bahnemann, *Chem. Rev.*, 1995, **95**, 69-96.
22. H. Ibrahim and H. de Lasa, *AIChE Journal*, 2004, **50**.
23. J. Arana, A. Pena Alonso, J. M. Dona Rodriguez, G. Colon, J. A. Navio and J. Pérez Pena, *Appl. Catal. B*, 2009, **89**, 204-213.
24. M. Pelaez, N. T. Nolan, S. C. Pillai, M. K. Seery, P. Falaras, A. G. Kontos, P. S. M. Dunlop, J. W. J. Hamilton, J. A. Byrne, K. O'Shea, M. H. Entezari and D. D. Dionysiou, *Appl. Catal. B*, 2012, **125**, 331-349.
25. A. Mills and H. S. Le, *J. Photoch. Photobio. A*, 1997, **108**, 1-35.
26. A. Fujishima, X. Zhang and D. A. Tryk, *Surf. Sci.Rep.*, 2008, **63**, 515-582.
27. R. Asahi, T. Morikawa, T. Ohwaki, K. Aoki and Y. Taga, *Science (Washington, DC, U. S.)*, 2001, **293**, 269-271.
28. X. Z. Li and F. B. Li, *Environ. Sci. Technol.*, 2001, **35**, 2381-2387.
29. I. recomendations, *Glossary of terms used in photochemistry*, 1996.
30. M. Grätzel, *J. Photoch. Photobio. C*, 2003, **4**, 145-153.
31. Y. Hu, D. Li, Y. Zheng, W. Chen, Y. He, Y. Shao, X. Fu and G. Xiao, *Appl. Catal. B*, 2011, **104**, 30-36.
32. A. Kudo and Y. Miseki, *Chem. Soc. Rev.*, 2009, **38**, 253-278.
33. Y. Park, K. J. McDonald and K.-S. Choi, *Chem. Soc. Rev.*, 2013, **42**, 2321-2337.
34. H. Jiang, H. Dai, X. Meng, K. Ji, L. Zhang and J. Deng, *Appl. Catal, B*, 2011, **105**, 326-334.

35. H. Jiang, H. Dai, X. Meng, L. Zhang, J. Deng, Y. Liu and C. T. Au, *J. Environ. Sci. (Beijing, China)*, 2012, **24**, 449-457.
36. H. Jiang, X. Meng, H. Dai, J. Deng, Y. Liu, L. Zhang, Z. Zhao and R. Zhang, *J. Hazard. Mater.*, 2012, **217-218**, 92-99.
37. H.-q. Jiang, H. Endo, H. Natori, M. Nagai and K. Kobayashi, *J. Eur. Ceram. Soc.*, 2008, **28**, 2955-2962.
38. P. U. M. Garcia, S. Sepulveda-Guzman, l. C. A. Martinez-de and M. U. Ortiz, *J. Mol. Catal. A-Chem.*, 2011, **335**, 169-175.
39. U. M. Garcia-Perez, S. Sepulveda-Guzman and l. C. A. Martinez-de, *Solid State Sci.*, 2012, **14**, 293-298.
40. U. M. Garcia-Perez, S. Sepulveda-Guzman, l. C. A. Martinez-de and J. Peral, *Int. J. Electrochem. Sci.*, 2012, **7**, 9622-9632.
41. S. Tokunaga, H. Kato and A. Kudo, *Chem. Mater.*, 2001, **13**, 4624-4628.
42. Z. Zhao, Z. Li and Z. Zou, *Phys. Chem. Chem. Phys.*, 2011, **13**, 4746-4753.
43. A. Walsh, Y. Yan, M. N. Huda, M. M. Al-Jassim and S.-H. Wei, *Chem. Mater.*, 2009, **21**, 547-551.
44. G. Xi and J. Ye, *Chem. Comm.*, 2010, **46**, 1893-1895.
45. Z. Zhang, W. Wang, M. Shang and W. Yin, *Catal. Commun.*, 2010, **11**, 982-986.
46. K. Rajeshwar and T. N. R. de, *Chem. Soc. Rev.*, 2009, **38**, 1984-1998.
47. B. Cheng, W. Wang, L. Shi, J. Zhang, J. Ran and H. Yu, *Int. J. Photoenergy*, 2012, 797968, 797910 pp.
48. L. Dong, S. Guo, S. Zhu, D. Xu, L. Zhang, M. Huo and X. Yang, *Catal. Commun.*, 2011, **16**, 250-254.
49. X. Zhang, Z. Ai, F. Jia, L. Zhang, X. Fan and Z. Zou, *Mater. Chem. Phys.*, 2007, **103**, 162-167.
50. Y. Guo, X. Yang, F. Ma, K. Li, L. Xu, X. Yuan and Y. Guo, *Appl. Surf. Sci.*, 2010, **256**, 2215-2222.
51. Y. Liu, H. Dai, J. Deng, L. Zhang and C. T. Au, *Nanoscale*, 2012, **4**, 2317-2325.
52. C.-Y. Chung and C.-H. Lu, *J. Alloys Compd.*, 2010, **502**, L1-L5.
53. B. Xie, C. He, P. Cai and Y. Xiong, *Thin Solid Films*, 2010, **518**, 1958-1961.
54. M. Wang, Q. Liu, Y. Che, L. Zhang and D. Zhang, *J. Alloys Compd.*, 2013, **548**, 70-76.
55. C. H. Hervoches, M. C. Steil and R. Muccillo, *Solid State Sci.*, 2004, **6**, 173-177.
56. F. A. Cotton and G. Wilkinson, *Advanced Inorganic Chemistry*, Jhon Wiley & Sons, 1988.
57. X. Chen and S. S. Mao, *Chem. Rev.*, 2007, **107**, 2891-2959.
58. G. H. Stout and L. H. Jensen, *X-Ray structure determination. A practical guide.*, Macmillan Publishing Co., 1968.
59. H. Yanagida, K. Koumoto and M. Miyayama, *The Chemistry of Ceramics*, Wiley and Maruzen, 1996.
60. D. S. Kim, S. H. Han and K. S.Y., *J. Colloid Interf. Sci.*, 2007, **316**, 85-91.
61. D. S. Kim and K. S.Y, *Appl. Catal. A*, 2007, **323**, 110-118.
62. T. Peng, *J. Phis. Chem. B*, 2005, **109**, 4947-4952.
63. F. Fresno, *Sintesis, caracterizaciòn y actividad fotocatalitica de TiO2 nanocrystalino dopado con Sn.*, Universidad Autònoma de Madrid, Ph. D Thesis, 2006.
64. D. Briggs and M. P. Seah, *Practical Surface Analysis - Volume 1 - Auger and X-Ray Photoelectron Spectroscopy, 2nd Ed.*, John Wiley & Sons, 1990.
65. N. Myung, S. Ham, S. Choi, Y. Chae, W. Kim, Y. J. Jeon, K. Paeng, W. Chanmanee, N. R. de Tacconi and K. Rajeshwar, *J. Phys. Chem. C*, 2011, **115**, 7793-7800.
66. Z. Özlem Kocabaş-Ataklı and Y. Yürüm, *Chem. Eng. J.* , 2013, **225**, 625-635.
67. P. Atkins and J. de Paula, *Physical Chemistry*, Oxford University Press, 2006.
68. M. Munowitz, *Principle of Chemistry*, W. W. Norton & Company, 2000.
69. U. Cernigoj, M. Kete and S. U. Lavrencic, *Catal. Today*, 2010, **151**, 46-52.

70. M. Tasbihi, U. Lavrenčič Štangar, U. Černigoj, J. Jirkovsky, S. Bakardjieva and N. Novak Tušar, *Catal. Today*, 2011, **161**, 181-188.
71. C. Antoine, *Comptes Rendus des Seances de l'Academie des Sciences*, 1888, **107**, 681-684, 778-780, 836-837.
72. N. A. Lange, *Lange's Handbook of Chemistry*, McGraw-Hill, New York, 1979.
73. K. i. Ishibashi, A. Fujishima, T. Watanabe and K. Hashimoto, *J. Photoch. Photobio. A*, 2000, **134**, 139-142.
74. B. E. Warren, *X-ray diffraction*, Dover, 1990.
75. J. F. Moulder, W. F. Stickle, P. E. Sobol and K. D. Bomben, *Handbook of X-Ray Photoelectron Spectroscopy*, Physical Electronics Inc., 1995.
76. P. van der Heide, *X-ray Photoelectron Spectroscopy: An Introduction to Principle and Practices*, Jhon Wiley & Sons, 2011.
77. K. D. Schroder, *Semiconductor material and device characterization*, John Wiley & Sons, 2006.
78. S. Brunauer, P. H. Emmett and E. Teller, *J. Am. Chem. Soc.*, 1938, **60**, 309-319.
79. N. I. Levine, *Fisicoquimica*, McGraw-Hill, 1996.
80. S. Brunauer, L. S. Deming, W. E. Deming and E. Teller, *J. Am. Chem. Soc.*, 1940, **62**, 1723-1732.
81. S. J. Gregg and K. S. W. Sing, *Adsorption, Surface Area and Porosity*, Academic Press, 1982.
82. K. J. Laidler, *Chemical Kinetics*, Pearson Education, 2004.
83. D. A. Skoog, F. J. Holler and S. R. Crouch, *Chimica Analitica Strumentale*, EdiSES, 2009.
84. H. H. Perkampus, *Encyclopedia of Spectroscopy*, VCH, 1995.

Acknowledgements

The most sincere thanks go to my relator, Silvia Gross (IENI-CNR, Dip. Di Scienze Chimiche, Università di Padova) as well as my correlator, Fernando Fresno Garcia (Laboratory of Environmental Research, University of Nova Gorica, Slovenia), for their support during the work, for their explanations and for their patience.

The Erasmus-Socrates European Union program and Università degli Studi di Padova are thanked for the financial support.

Wholehearted thanks go to Urška Štangar Lavrenčič, (Dean of the University of Nova Gorica) for accepting me in her group, and for the opportunities offered to me.

I gratefully thank all the members of the Italian group, Giulia Morgese, Marilisa Vigolo, Paolo Dolcet, Erika Butturini and Gabriele Dal Ben for their company and the good time spent together. In particular I have to thank Stefano Diodati, for his corrections, explanations and translations.
The same thanks go to all the people met in the Nova Gorica University, who gave me all the assistance I needed and make me feel at home during my stay abroad.

I want to express all my gratitude to all people that helped me aside the university framework, but whose support was fundamental in many different ways: my parents Vanna and Paolo, my boyfriend Luca, my relatives and all my friends.